npj | climate and atmospheric science

Article

Published in partnership with CECCR at King Abdulaziz University

https://doi.org/10.1038/s41612-025-01023-x

Increasing probability of extreme rainfall preconditioned by humid heatwaves in global coastal megacities

Poulomi Ganguli[1] ✉ & Bruno Merz[2,3]

Hot–wet compound events, the sequential occurrence of humid hot days followed by extreme rainfall, can cause catastrophic consequences, often exceeding the impacts of the isolated occurrence of each event. The urban-coastal microclimate is confounded by complex interactions of land–sea breeze circulations, urban effects of convection and rainfall, and horizontal advection of moisture, which can favor the hot–wet compound occurrence. We present the first observational assessment (1951–2022) of summertime hot–wet compound events across global coastal megacities. We find a significant ($P < 0.001$) increase in the frequency of hot–wet compound events in both hemispheres: on average, ~3 events in the 1950s to 43 events in the 2020s. Cities with upward trends in the frequency of hot–wet compound events are situated < 30 km from coasts, with cities in the southern hemisphere showing faster hot-to-wet transition times (<3 days) than cities in the northern hemisphere. Further, 26 out of 29 sites show increased extreme precipitation, reaching 153%, when humid heat amplitude rises from the 50th to 90th percentiles. Understanding hot–wet compound interactions over the world's coasts is highly relevant for climate change impact assessment and informing climate adaptation.

Most megacities are located in the coastal zone, with about 40% of the world's population residing within 100 km of the coast[1]. Globally, coastal areas are at increased risk of flooding due to relative sea level rise, land subsidence, and altered storm intensity and frequency[2–4]. In addition, the world coastlines are also hotspots of humid heat stress[5]. Increased urbanization can alter the wind direction in coastal areas due to changes in the density and height of buildings, which reduces the sea breeze in the fall, whereas increased surface temperature at night in urban areas often leads to decreased land breeze[6]. Observations showed a latitudinal pattern of heatwaves over the coasts with a robust increase in severity in the past decades due to increasing air temperature and reduced wind speed, often leading to slower-moving heatwave events, elevating the risk of ecosystem productivity reduction, rising energy consumption, and capacity needs[7]. Further, coastal heatwaves are often accompanied by persistent high sea surface temperature, resulting in exposure to high temperature and humidity in cities close to coasts[8]. Moreover, globally, coastal precipitation peaks in the boreal summer[9]. The superposition of heat stress, humidity, and precipitation may lead to hot–wet compound events—the sequential occurrence of humid hot days and extreme rainfall. Such events can pose a significant threat to coastal communities and cause greater damage than the isolated occurrence of either of these extremes. For instance, a heatwave could massively increase the number of people who need medical assistance and trigger power blackouts[10]. In such a vulnerable period, extreme rainfall and flooding could place additional stress on the critical infrastructure[2,11], for instance, by interrupting traffic and water provision.

During summer, temperature and precipitation are generally anticorrelated over the interior part of the continent but positively correlated over oceans and near the coasts[12,13]. Coasts are transition areas where local characteristics also affect the interplay between temperature, humidity, and precipitation. Extreme humid heatwaves often lead to high atmospheric instability and moisture convection, increasing the likelihood of precipitation extremes[14]. High atmospheric instability, moisture, and frontal systems jointly mediate rainfall extremes that follow heatwaves[15]. There is growing evidence of the co-occurrence of humid heatwaves and extreme precipitation in several regions from observations, such as in China[16–21], India[14], Australia[22], and the USA[23], and global climate projection scenarios[24–26]. These assessments, however, are limited to either smaller spatial domain focusing on particular country[19–21] or coarse-resolution gridded observations [e.g., 0.5° spatial resolution in CRU grid-based observations in Europe[27] and China[21,28], and 2.5° observational records from the India

---

[1]Indian Institute of Technology Kharagpur, Kharagpur, India. [2]GFZ Helmholtz Centre for Geosciences DE, Potsdam, Germany. [3]Institute for Environmental Sciences and Geography, University of Potsdam, Potsdam, Germany. ✉e-mail: pganguli@agfe.iitkgp.ac.in; poulomizca@gmail.com

Meteorological Department over the Indian Mainland[29], ERA5 re-analysis based runs as a proxy for observations over the Mediteranean[30], Germany[31] and China[18], and coupled model intercomparison phase 6 (CMIP6) climate model outputs over the entire globe[32–36]. Re-analysis data, which are often used as a proxy for observations, show large biases in relative humidity[37], a key element to determine humid heat. Extreme humid heatwaves are highly localized in space and time, and their peaks are typically underestimated by re-analysis products and climate models (Fig. S11 in Raymond et al. [38] and Freychet et al. [39]). Likewise, re-analysis products often over/underestimate summer precipitation extremes[40,41], despite their ability to simulate the annual and seasonal patterns of observed precipitation. Further, a notable bias of CMIP6 models in simulating the magnitude of precipitation extremes has been found for the tropics, arid and semi-arid regions, in particular for the South Asian and West African monsoon seasons[42,43]. Although several studies have assessed projected changes in hot–wet compound events using the latest generation climate models (e.g., CMIP6 in refs. 26,32–35,44), they have considered large spatial domains, such as the national scale or the entire globe, without considering finer-scale features. They have often relied on coarser spatial (1–2.8°) and temporal (often monthly) resolutions. For the coasts, the results of these studies need to be interpreted with caution since they often fail to capture small-scale but important details, such as local coastlines and orography, which influence thermal gradients and rainfall patterns[45].

Several studies have investigated hot–wet compound events, but they have not specifically examined the distinct characteristics of these events at the coasts[15,16,22,36,46]. Coastal cities, which have generally more moderate climates than inland cities, can experience severe consequences from hot–wet compound events[14]. They can lead to complex hazards that damage coastal infrastructure, alter coastline features, and disrupt ecosystems. Climate change alters the timing of the individual drivers of hot–wet compound events, thereby affecting the response times (i.e., delay between two peaks) of humid heatwaves and the following extreme precipitation, which impacts the frequency of such events. To our knowledge, hot–wet compound events have not been investigated so far across densely urbanized global coastal megacities, particularly in the tropics, which are hotspots of deadly humid heat stress[47,48]. Previous analyses emphasizing coastal areas have either focused solely on humid heat stress[8] or examined interactions between wind and precipitation extremes[49], as well as heatwaves—extreme sea levels[50]. Using reanalysis and observations, so far, only a few studies have investigated hot–wet compound events on a global and continental scale. Sauter et al. [15,46] used hourly rainfall observations from the global sub-daily rainfall dataset[51] and reanalysis-based ERA5 temperature datasets to investigate mechanisms behind hot–wet compound events across Australia, Japan, the United States, Central and Southern Europe, and India. You et al. [36] used coarse resolution (2.5° × 2.5°) re-analysis-based gridded time series to analyze hot–wet compound events at a global scale. However, trends in the frequency and the timing of both extremes, which may alter the response time between the two extremes, remain poorly understood. Short response times, characterized by the quick succession of a humid heatwave followed by intense rainfall, pose significant challenges for disaster management. The rapid shift from hot to wet conditions in densely populated, low-lying coastal areas poses a substantial risk to environmental planning and resource allocation. Therefore, understanding the covariability between humid heat stress and subsequent rainfall will help to provide more credible multi-hazard risk assessments, improving monitoring and real-time forecasting of such events.

To fill these knowledge gaps, we address the following research questions, specifically for coastal megacities: (1) Does the timing, i.e., the occurrence throughout the year, of the singular and the compound hot–wet events change over time, and how does this change affect the response time? (2) Does the frequency of hot–wet compound events change? (3) How does the likelihood of extreme precipitation preconditioned by humid heat change with increasing heat stress levels? Here, we develop the first observational assessment (1951–2022) of hot–wet compound event characteristics, such as frequency, response time, and timing, during the warm season over global coastal megacities (Fig. 1 and Table S1). By utilizing ground-based observations, our study provides more reliable insights into hot–wet compound events across coastal megacities, aiding in the evaluation of climate models for impact assessment, and complementing ongoing efforts on large-scale compound event assessments[52,53]. This research supports coastal hazard management and mitigation efforts and identifies hotspot locations along the coasts where humid heatwaves and extreme rainfall are a recurring problem.

Results

Frequency of hot–wet compound events across coastal megacities

The frequency of hot–wet compound events shows distinct regional differences across global coastal megacities (Fig. 1). About 62% of sites (18 out of 29) show more than one hot–wet compound event/year. Hot–wet compound events are most prevalent across the coasts of Southeast Asia and the northeastern United States, except for Taipei, with the frequency exceeding 2 events/year. The highest frequency of hot–wet compound occurrence was observed in Miami in the northeastern USA, with 2.6 events/year, followed by Bangkok in Thailand, with 2.28 events/year. Cities with rare compound events (<0.5 events/year) include San Francisco in the Pacific Northwest, Antalya in Turkey with a Mediterranean climate, and Casablanca in Northwest Africa with a mild Mediterranean climate. All three cities demonstrate asynchronous patterns in the timing of heatwave peaks and extreme rainfall. Heatwave peaks typically occur in June and July, while extreme rainfall tends to peak in January. As a result, hot–wet compound events are rare in these cities.

Trends in mean timing of singular climate stressors vs hot–wet compound events

In the northern hemisphere, the mean timing of humid heatwaves (Fig. 2a) is primarily concentrated in June, followed by July. In the southern hemisphere, humid heatwaves occur on average from December to January. The highest values of wet-bulb temperature (median of around 29 °C) are found close to 20° N latitude. Heatwave amplitudes decrease strongly towards the Arctic and more gradually towards the Antarctic.

Rainfall extremes (Fig. 2b) occur on average in July in monsoon-dominated Asia and South Africa, where the summer accounts for at least 55% of total annual precipitation[54]. In the humid subtropical areas of North America, for example, in Washington DC and Miami, where summers are typically long, hot, and humid, rainfall extremes also tend to occur in July. In the extra-tropical region (≥30°) over Europe, the mean timing of extreme precipitation varies between July and November. Over the hot-summer Mediterranean region[55], in the Middle East and the Pacific northwest United States, the mean timing of extreme precipitation is primarily concentrated in the winter season (December–February). Extreme rainfall across the Pacific Northwest United States during the cool season is mainly attributed to landfalling atmospheric rivers that can produce heavy orographic precipitation during the passage of mountainous areas of mid-latitude regions[56,57]. In the humid subtropical climate regions of the southern hemisphere, i.e., along the coasts of Australia and South America, the mean timing of extreme precipitation is mainly during January–March, with the exception along the New Zealand coast in Auckland, where extreme rainfall mainly occurs in winter (June). This could be a consequence of the frequent atmospheric rivers in winter (June–August)[58]. The changes in precipitation extremes with latitude are more erratic compared to the changes in heatwave amplitude. The highest values (~45 mm/day) are found around 20° N, roughly at the same latitudes where the highest heatwave amplitudes occur.

The trends in mean timing of humid heatwaves (Fig. 3) show a statistically significant delay over 52% of sites (15 out of 29), especially over extra-tropical regions and southern Europe, the eastern Mediterranean region, the northwest coast of Africa, and the Pacific northwest coast of California in the northern hemisphere. Most of the sites in the southern hemisphere show a significant delayed arrival of humid heatwaves except for Rio de Janeiro, where the delay is statistically insignificant. Earlier

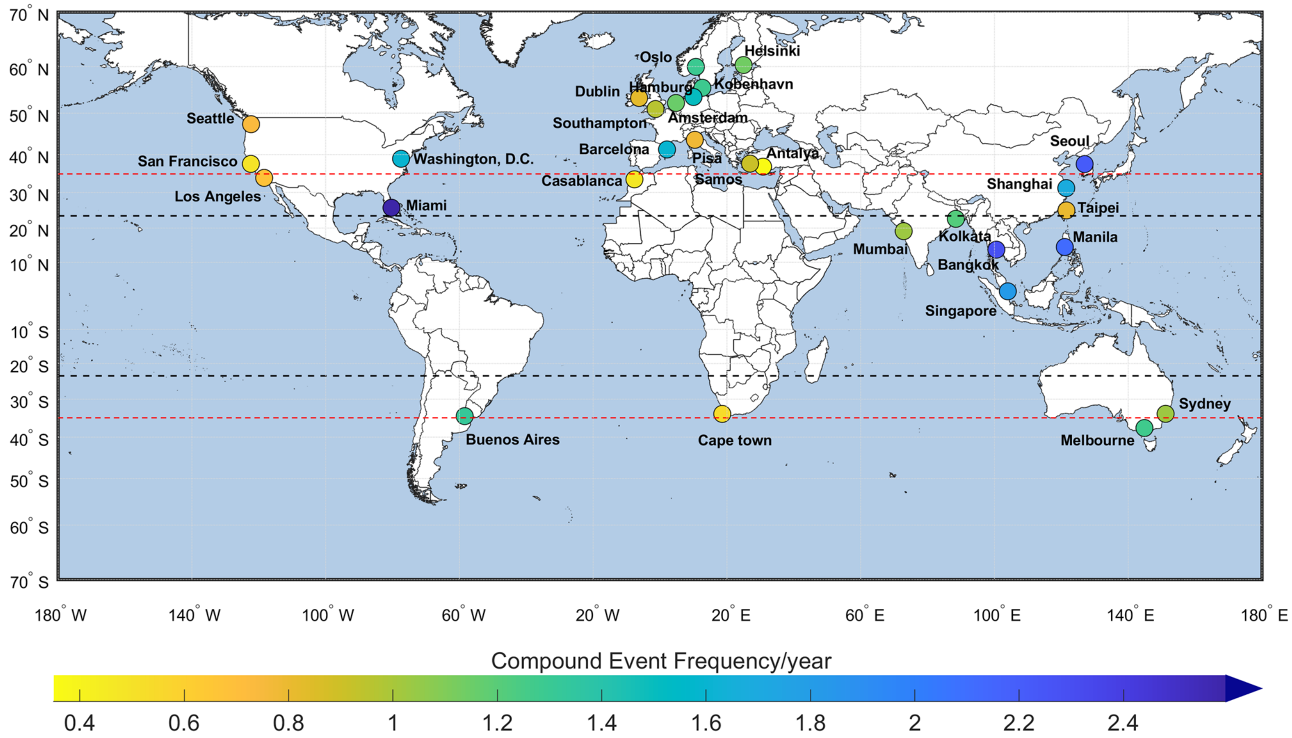

Fig. 1 | Locations of 29 megacities near the sea. Shades of the circle show the occurrence frequency of 'hot–wet' compound events determined by total event frequency during the analysis period (1951–2022) divided by the common number of years available for temperature and precipitation observations. A hot–wet compound event is sampled when an extreme precipitation follows a humid heatwave within a time window $t \in (-1, 7)$ days (see "Methods" for details). The area encompassed within ±23.5° N (S) demarcates the tropics (dashed black lines). Likewise, areas within 23.5° N to 35° N (−23. 5 to −35° S) show the northern (southern) subtropical region (dashed red lines).

arrivals of humid heatwaves are found at only 10% of the sites (3 out of 29), and all these trends are statistically insignificant. The probability density function (PDF) of trends in the mean timing in humid heatwaves shows a distinct asymmetry with an elongated right tail of up to 3% decade^{-1}, equivalent to 5.6 days/decade^{-1}.

The trends in the mean timing of precipitation extremes (Fig. S1) are subtle and range from −0.1 to +0.09 days/decade, which is much smaller compared to trends in the mean timing of humid heatwaves. Like the heatwaves, a higher number of sites (59%; 17 out of 29) show a delayed arrival of precipitation extremes, particularly sites in the subtropics and mid-latitudes of the northern hemisphere. For two coastal megacities, Manila in the Philippines and Alexandria in Egypt, we find a statistically significant trend towards earlier arrival of precipitation extremes. Most sites in the southern hemisphere show a delayed arrival of precipitation extremes.

The mean timing (Fig. 4) of hot–wet compound events is primarily clustered in June, during which >40% (12 out of 29) of sites experience humid heat-extreme rain events. These sites are typically located on the Atlantic coasts of Europe and North America, while on the Pacific coast, the mean timing occurs from April to May. Across the northern hemisphere, the mean timing of hot–wet compound events is distributed from March to August, while in the southern hemisphere, the mean timing is clustered between December and January.

The trends in the timing of hot–wet compound events (Fig. 5) are mainly delayed. Around 80% (23 out of 29) of sites show a delayed arrival of hot–wet compound events, with an average of 6 days/decade. The sites with significantly delayed timing are primarily concentrated across midlatitudes in both hemispheres, ranging from 4.23 to 15.6 days/decade. A few sites, mainly in the tropics, show an earlier arrival of hot–wet compound events, ranging from −0.32 to −3.6 days/decade, although none of these trends is statistically significant. Further, the trends in the timing of humid heat (>40% of gauges showing delays exceeding 5 days/decade) have a larger influence on the trends in the timing of hot–wet compound events compared to trends in the timing of extreme rainfall.

Megacities are susceptible to hot–wet compound events

To identify hotspots that are susceptible to the sequential occurrence of hot–wet compound events, we quantify (i) the upper tail dependence strength between the two extremes, (ii) the average annual frequency of hot–wet compound events, (iii) trends in response times, i.e., the elapsed time between the sequential events; and (iv) precursor coincidence rates to assess the fraction of precipitation extremes that are preceded by humid heatwave amplitudes within $\Delta T = 7$-day time window (see "Methods"). The map of upper tail dependence between heatwave amplitude and extreme rainfall (Fig. 6a) shows statistically significant dependence for 41% of the sites (12 out of 29) with a median value of around 0.2. The highest upper tail dependence (0.53) and P-value of 0.015 is found for Cape Town in South Africa. Further, around 24% of the sites (7 out of 29) experience > 2 compound events/year. Manila in the Philippines, followed by Miami on the eastern North American coast, shows the largest annual frequency of hot–wet compound events; both reported > 3 events yearly.

The mean response times of hot–wet compound events (Fig. 6b) vary from around 2 days to over 5 days. 31% of the sites (9 out of 29) have a mean response time of >3.5 days. These gauges are primarily located in the tropics and mid-latitudes. Thirty-four percent of the sites (10 out of 29) show mean response times of <3 days, indicating a rapid transition from the humid heatwave to the precipitation extreme. These sites are located between 34° and 60° in both hemispheres. This is in agreement with an earlier assessment[15], which showed that extreme rainfall following a heatwave is more likely in mid to high latitudes than elsewhere. These regions are characterized by temperate to polar climates with high temperatures and high moisture during the summer, providing a favorable condition for high atmospheric instability and moisture during heatwave termination. The mean response time of sites in the southern hemisphere is relatively short

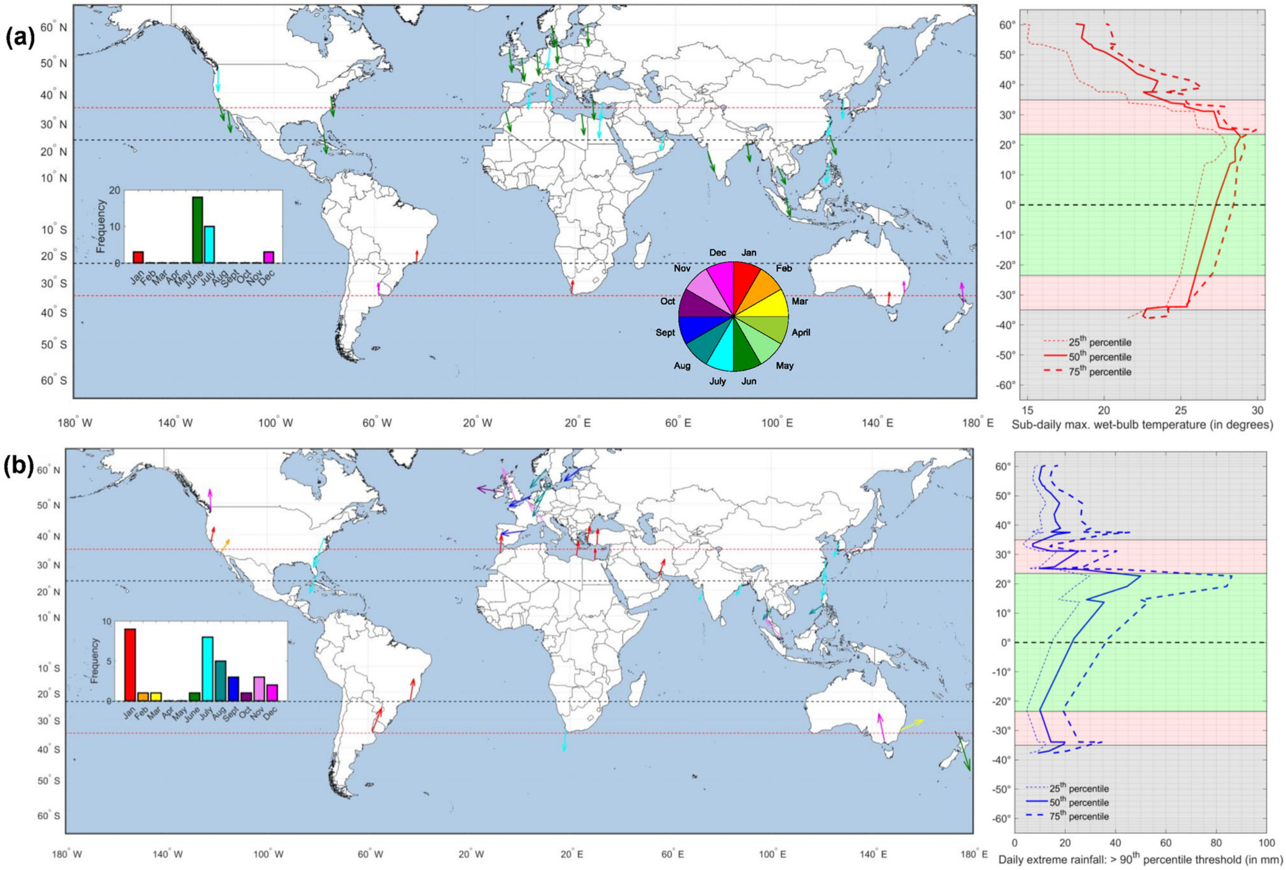

Fig. 2 | Mean timing of singular events. a Mean timing of humid heatwaves. The histogram in the inset shows the global distribution of the frequency of humid heatwave amplitude in different months, with shades indicating mean timing. The arrow length is proportional to the variability in the event timing—a small (large) arrow length indicates low (high) variability. The arrow direction indicates the mean timing of the event in terms of the day of the year counted from 1st January, whereas the shade shows the mean month (or the season) of occurrence. Right panel: latitudinal transect showing the distribution of humid heatwave amplitudes across temperate (gray), subtropical (pink), and tropical (green shades) climate regions. The median and interquartile range of heatwave amplitudes are derived from the heatwave amplitude of all heatwave episodes for a given site. **b** Mean timing of extreme precipitation. The inset shows the global distribution of the monthly frequency of extreme precipitation. The shades on the pie charts apply to both panels and indicate the mean timing of the events. Right panel: same as in Fig. a, but for extreme precipitation.

and often <3 days. The distribution of response times of hot–wet compound events for the sites in the southern hemisphere shows a skewed distribution with a mean value of <2 days (Fig. 6b, inset). In contrast, the mean response times of sites in the northern hemisphere have a relatively flat distribution. The mean response times at northern hemisphere gauges vary from 2.5 days to 5.25 days, whereas the mean response times in the southern hemisphere are smaller than 3 days for all four cities. Our finding of small transition times for sites across southern Australia agrees with Sauter et al. [15], who showed a high likelihood of extreme rainfall following heatwaves due to the predominance of frontal systems driving the rainfall extremes. The transitions from hot-to-wet compound events closely follow the mean timings of the heatwaves and extreme precipitation, leading to shorter or longer response times. Trends in response times are mostly insignificant (Fig. 6b). Only at two sites in the mid-latitudes, i.e., Hamburg in Germany and Southampton in the United Kingdom, we detect statistically significant ($P > 0.95$) increasing trends. Four sites, located in the subtropics and close to the subtropical climate region, show a statistically significant ($P < 0.05$) decreasing trend in response times.

Next, the precursor coincidence rate between humid heatwaves and precipitation extremes varies between 1.4% and 5.1% in the northern hemisphere and between 4.2% and 5.7% in the southern hemisphere (Fig. 7a). This means that around 3% and 5% of all humid heatwaves are followed by an extreme rainfall event in the northern and southern hemisphere, respectively. While the likelihood of sequential occurrence of hot–wet compound events is higher over the selected sites across the southern hemisphere, the northern hemisphere sites show a higher variability. The highest coincidence rate (5.1%) is observed in Singapore, followed by Shanghai (4.9%). The lowest rates are found for Casablanca (1.4%) and Taipei (1.7%), both sites located in the northern hemisphere sub-tropics. All four gauges in the southern hemisphere show a precursor coincidence rate of >4%, with the highest value (5.7%) in Buenos Aires and Melbourne. All four sites are located within a 20 km radius of the coastline. Sites with higher (>3%) coincidence rates are clustered around less than 30 km radius from the coastline (Fig. 7b). However, a few coastal megacities with >10 M inhabitants (17%, 5 out of 29) show precursor coincidence rates of >3%, despite being further from the coast. Hence, the scatterplot between precursor coincidence rate versus distance of megacities from the coastline suggests a highly nonlinear relationship, which is probably a consequence of local influences, such as local land–sea feedback processes.

Growing frequency of hot–wet compound events in recent periods

Over the northern hemisphere, the frequency of hot–wet compound events during the boreal summer shows an increasing trend ($P < 0.001$) at the rate of 0.18 $\text{decade}^{-1}\text{station}^{-1}$ during the period 1950–2022 (Fig. 8a, upper panel). The total number of hot–wet compound events increased from ~2 events in the early 1950s (i.e., 0.08 events per station and year) to 37 events in the 2020s (i.e., 1.48 events per year and station). The 90th percentile

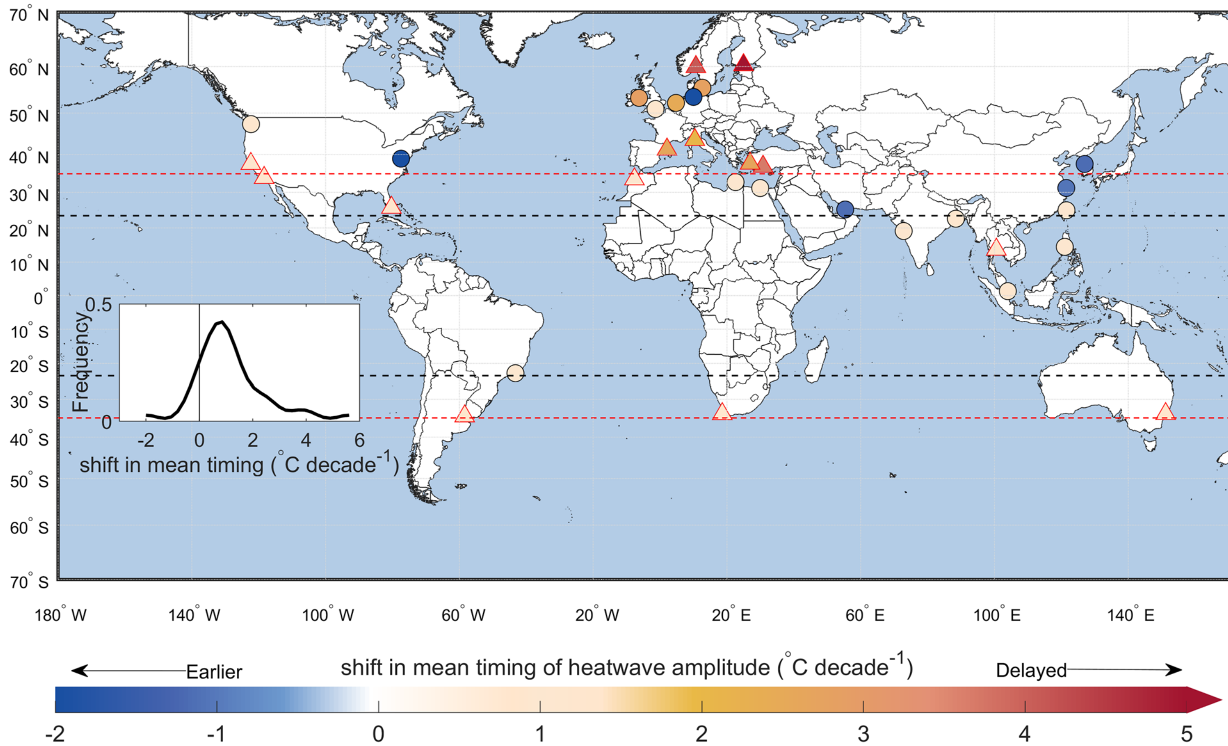

Fig. 3 | Shift in the mean timing of humid heatwaves. The inset shows the frequency of the long-term trend in the timing of humid heatwaves. Statistical significance of shifts in timing was evaluated via a resampling-based approach with $N = 2000$ bootstrap runs. Significance of trends is reported at P-value < 0.05 for earlier onset and P-value > 0.95 for delayed arrival of events. Upward triangles show significant delays, downward triangles show significant earlier arrivals; circles show insignificant changes. Shades of the markers represent the change magnitude.

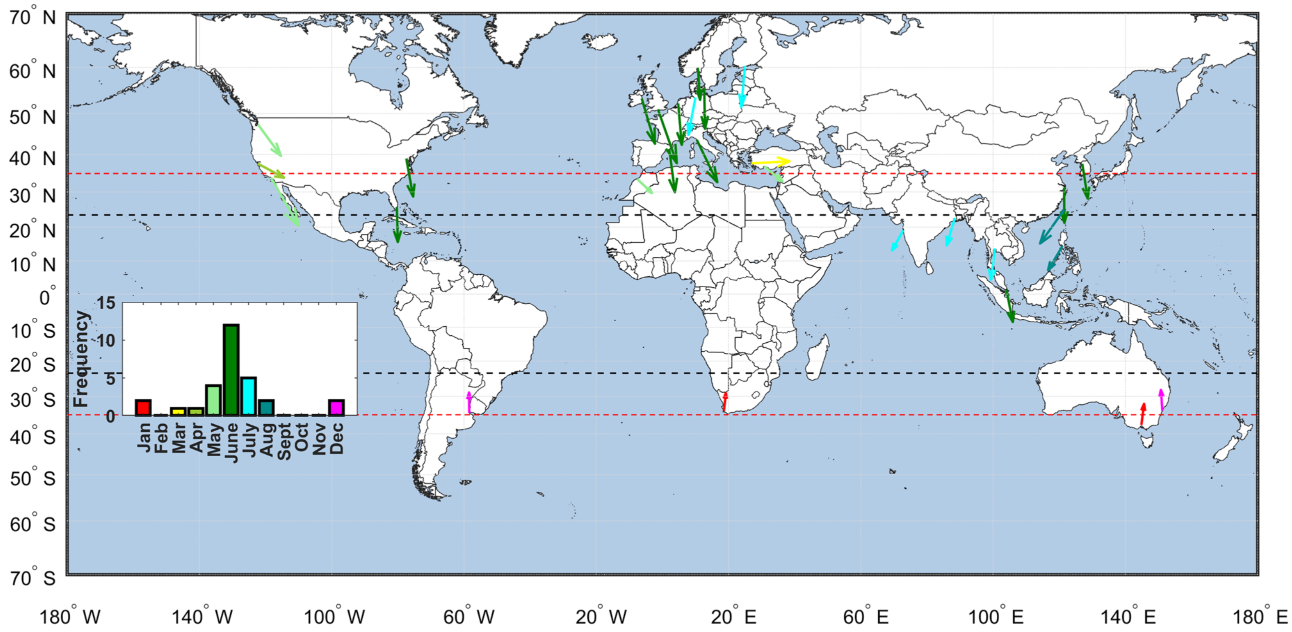

Fig. 4 | Mean timing of hot–wet compound events. The colors indicate the mean timing, and the arrow length is proportional to the variability in the event timing. The arrow direction indicates the mean timing of the event in terms of the day of the year counted from 1st January.

probability contour (Fig. S2, top panel) of the two-dimensional distribution of $AHWMI_d$ (Accumulated daily Heat Wave Magnitude Index) versus the standardized daily anomaly of the following rainfall using nonparametric kernel density estimator shows that in the tropics around 81% of the hot–wet compound events are associated with moderate to super-extreme humid heatwave events[59] that are followed by >1 − SD departure from mean rain events. Notable examples include the 1991 and 2003 heatwaves that resulted in >4 − SD extreme rainfall events in Mumbai on the western coast of India and in the Bangkok metropolitan area in Thailand, respectively. In 1987, 2002, and 2019, record-breaking high temperatures in

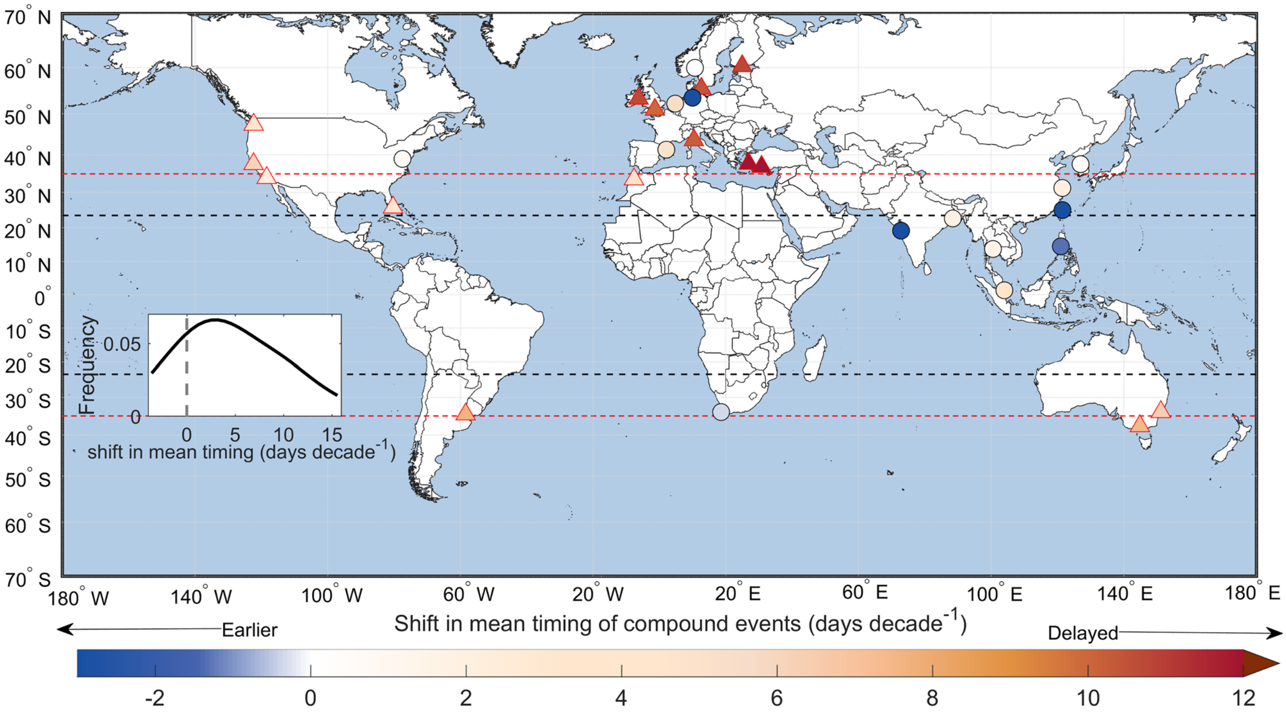

Fig. 5 | Trends in the mean timing of hot–wet compound events. The inset shows the frequency of the trend in timing. Statistical significance was evaluated via a resampling-based approach with $N = 2000$ bootstrap runs. Significance of trends is reported at P-value < 0.05 for earlier onset and P-value > 0.95 for delayed arrival of events. Upward triangles show significant delays, downward triangles show significant earlier arrivals; circles show insignificant changes. Shades of the markers represent the change magnitude.

Bangkok resulted in very-extreme to super-extreme humid heatwave events with $AHWMI_d$ values in the range 36.5—53.4. Two of these events (1987 and 2002) were associated with extreme rainfall of around $1-$SD. Over the mid-latitudes, only 20% (128 out of 638) of rain events with $>1-$SD departure from the mean rainfall are preceded by moderate to extreme humid heatwaves. Over the northern sub-tropics, ~8% (17 out of 207) rain events are associated with $<-1-$SD. The downward shift of the 90th percentile contour suggests that heatwaves in this region are more often associated with below-average rainfall events.

Over the southern hemisphere, the frequency of hot–wet compound events during summer shows a statistically significant increasing trend ($P < 0.001$) at a rate of 0.17 $\text{decade}^{-1}\text{station}^{-1}$ during the period 1975–2022 (Fig. 8a, lower panel). The total number of hot–wet compound events increased from ~1 event in the early 1980s (i.e., ~0.3 events per station and year) to 6 events in the 2020s (i.e., ~1.5 events per year and station). Like in the northern hemisphere, the 90th percentile probability contour of $AHWMI_d$ vs the standardized anomalies of the subsequent rainfall shows several extreme rainfall events that are associated with moderate to extreme humid heatwaves. Examples include Sydney in the subtropical southern hemisphere, where the 2001 and 2017 moderate heatwaves are followed by >4-SD rains. Another example is the 2017 event in Buenos Aires with rainfall > 2-SD departure from normal, which was preceded by an extreme humid heatwave with an $AHWMI_d$ value of ~17.

A three-way comparison between trends in frequency, distance to the coast, and population size (Fig. 8b) shows no clear relationships. The largest increase of 1.08 events/decade is observed for Manila, which is directly located at the coast, and there is a negative correlation (Spearman correlation: $\rho = -0.23$) between trend slope and distance to coast. However, this correlation is statistically insignificant. The correlation between trend slope and population size is also insignificant (Spearman correlation: $\rho = -0.005$).

Higher likelihood of extreme rainfall in response to warming

Figure 9 maps the relative changes in the exceedance probability of precipitation extremes ($P > p_{90}$) with an increase in heatwave amplitude from its median to 90th percentile sampled temperature extremes, considering humid heatwaves as the conditioning driver. We observe a modest (5%) to substantial (153%) increase in the exceedance probability of extreme precipitation as peak humid heat intensity increases from the 50th to the 90th percentiles. More than a 50% increase in extreme precipitation likelihood is observed across the four cities located between 33° and 44° (Pisa, Cape Town, and Casablanca in the Northern hemisphere and Melbourne in the Southern hemisphere). These cities are situated in or near the mid-latitudes, where high moisture levels, atmospheric instability following a heatwave, and frontal systems are likely to lead to extreme rainfall[15].

The highest increase (153%) is observed in Casablanca in northwest subtropical Africa, followed by Pisa (80% increase) in the northern temperate region. Melbourne (61%) in southeastern Australia shows the largest increase in exceedance probability among the sites in the southern hemisphere. We find substantial expected increases in precipitation extremes in response to an increase in peak humid heatwave amplitude, especially for sites located across the temperate and subtropical climate regimes. Our findings agree with earlier literature[15,16,46]. Humid heatwaves are associated with high temperature and high humidity. The high temperature increases the atmosphere's capacity to hold moisture. The increased moisture in the atmosphere can result in more condensed moisture, favorable for heavy rainfall. The heat forcing combined with moisture accumulation can contribute to atmospheric instability and trigger convection[36,60], leading to heavy rain after the end of a heatwave[16]. Additionally, the end of a heatwave can be associated with a shift from a large-scale atmospheric blocking to circulation anomalies with the passage of fronts and thunderstorms, which act as triggers for heavy rain[61]. Frontal systems can bring additional moisture and trigger convection. The areas that are most prone to hot–wet compound events are in non-arid mid and high latitudes, where high summer temperatures and abundant moisture are more common. These regions also tend to have more frontal systems[15]. Among the 29 global megacities, only two sites in the northern hemisphere, namely Singapore in the tropics and Los Angeles in the subtropics, show no change, whereas San Francisco, located in the mid-latitudes, shows a decrease in exceedance probability.

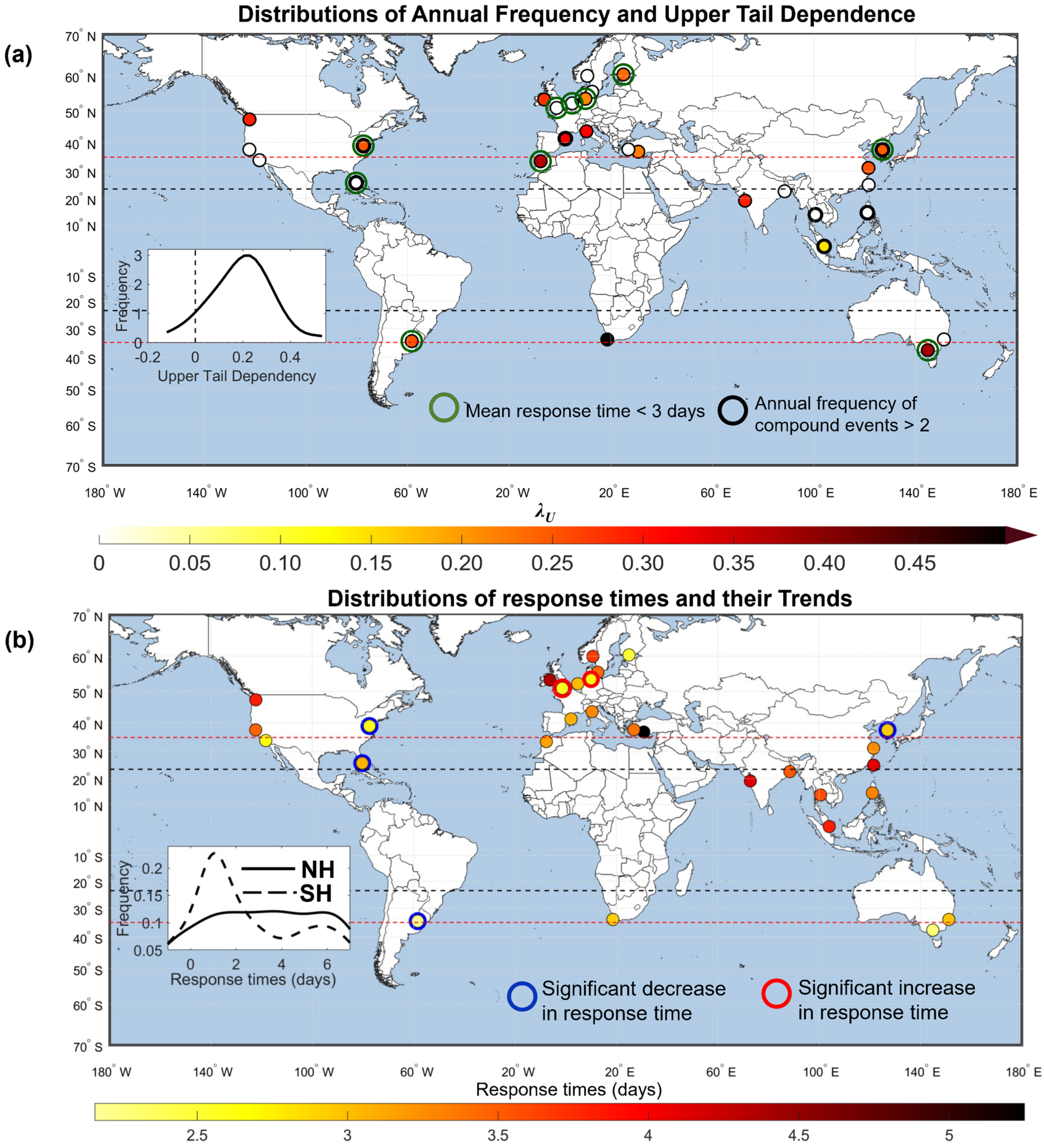

Fig. 6 | Spatial Distributions of Annual Frequency, Upper Tail Dependence, and Transition Times from Hot-to-Wet Compound Events. a Upper tail dependence between humid heatwave amplitude and extreme rainfall. Shaded markers, varying from light yellow to dark red, show statistically significant (P-value < 0.10) upper tail dependence, while white circles show either negative or insignificant upper tail dependence. The inset shows the distribution of upper tail dependence across the sites with a median value close to 0.2. **b** Spatial distribution of mean response (delay) time and trends in response times. A shorter response time represents a faster transition from the humid heatwave to the extreme rainfall. The edge colors in blue (red) in the circles indicate sites with significant decreases (increases) in response time. The inset compares the distributions of response times in the northern (in solid black line) vs southern (in dashed black line) hemispheres. While response times vary strongly across the northern hemisphere, most sites in the southern hemisphere show a response time of 1 day.

Regional differences and way forward

Our study has provided the first observational assessment of humid heatwave-extreme rainfall compound events for low-lying and densely populated coastal megacities. For the past seven decades and aggregated over all 29 sites, we find a significant increase in the number of hot–wet compound events, from ~3 events in the 1950s (rolling mean of 1950–1954) to ~43 events in the 2020s (rolling mean of 2016–2020). By fitting a copula-based conditional probability model, we show that for most of the sites (26 out of 29 megacities), the likelihood of extreme rainfall increases with increases in humid heatwave amplitudes. This could be because warmer air can contain more water vapor, which is a key ingredient for precipitation[46]

Sites across the southern hemisphere and the US eastern coast emerge as hotspots of hot–wet compound events owing to their shorter and often declining trends in response time and their high (>4%) summer precursor

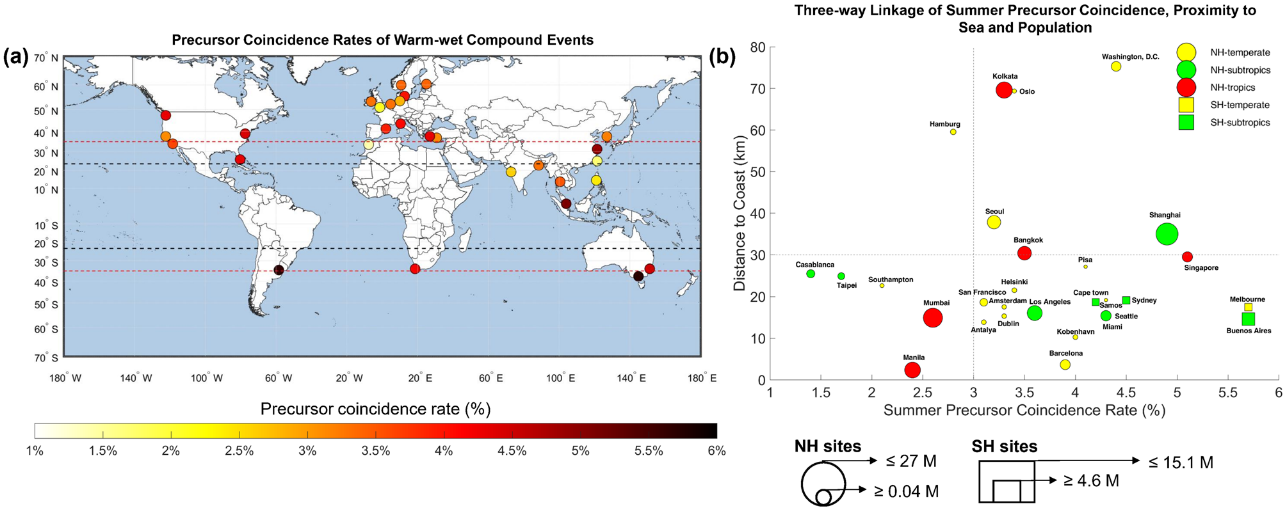

Fig. 7 | Precursor Coincidence Rates of Hot-Wet Compound Events and their Relationship with Distance to Coastline and Population. **a** Spatial distribution of the precursor coincidence rate of hot–wet compound events during the summer season. Statistical significance of event coincidence was evaluated using $N = 10,000$ bootstrap runs at a 5% significance level. **b** Precursor coincidence rate vs distance to coast. Circles (squares) indicate sites in the northern (southern) hemisphere; the size of the circle (square) is proportional to the population of the urban agglomerate in 2020. Shades of the marker indicate climate regions. NH and SH denote the northern hemisphere and southern hemisphere gauges.

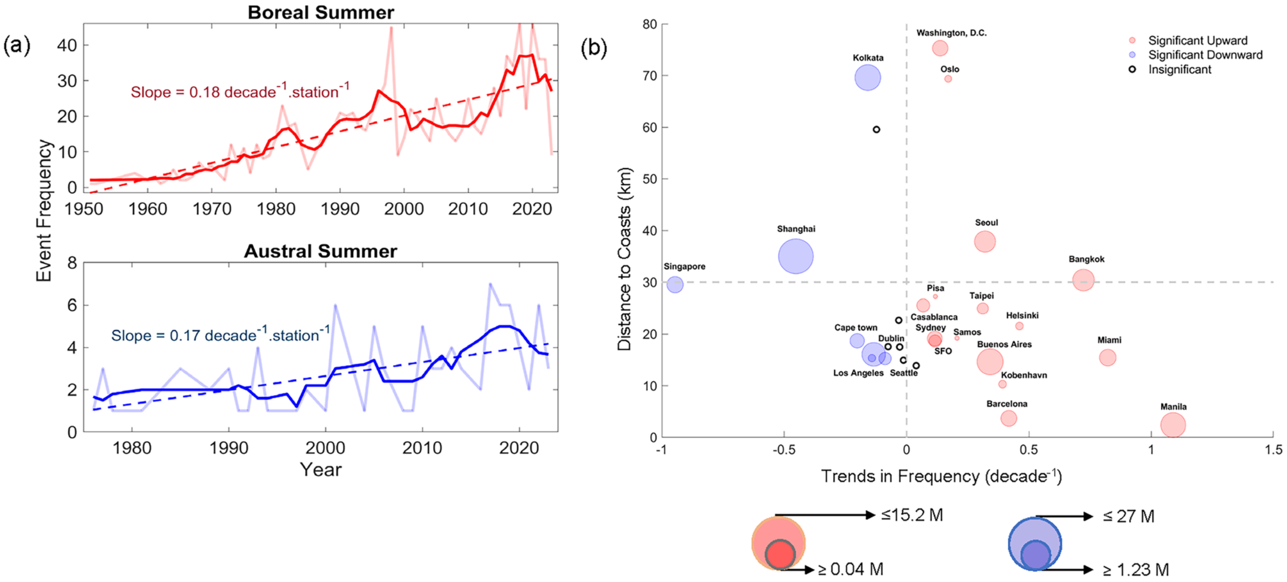

Fig. 8 | Trends in Frequency of Hot-Wet Compound Events and their Relationship with Distance to Coastline and Population. **a** Frequency of hot–wet compound events during summer in the (top panel) northern and (bottom panel) southern hemispheres. Shaded lines show the annual frequency. Solid lines show the smoothed frequency using a 5-year moving average to highlight the interannual to decadal variability. Trends in frequency using linear regression are shown using dashed lines. Both trends are statistically significant, with a *P*-value < 0.001 using the *F*-test. Trends are expressed in units of change in counts per decade (i.e., 10 years) per station to report trend estimates comparable across different sites with varied record lengths. **b** Trends in frequency of hot–wet compound events vs their distance from the coast. The trend in smoothed frequency (5-year moving window) of hot–wet compound events is determined using a least-squares regression fit. The size of the marker is proportional to the population of the urban agglomerate in 2020. Shades of the markers indicate significant upward and downward trends in hot–wet event frequency.

coincidence rates: Cape Town in South Africa and Melbourne in Australia show an increase of more than 50% in the exceedance probability of extreme rainfall in response to an increase in peak humid heat stress. Further, Buenos Aires and Sydney show significant upward trends in the frequency of hot–wet compound events with a 20–34% increase in exceedance probability of peak precipitation in response to an increase in peak humid heat stress. Likewise, Miami and Washington, DC show high summer precursor coincidence rates with significant decreasing trends in response times. Sites that emerged as ‘cold spots’ of hot–wet compound events show lower summer precursor coincidence rates and no significant changes or even increasing trends in response times. Those include a few sites in northwestern Europe (Hamburg and Southampton), North Africa (Casablanca), the Mediterranean (Antalya), and the western Indian subcontinent (Mumbai). In contrast, sites across the western Pacific coast, such as San Francisco and Los Angeles, show no changes or a modest decrease in precipitation peaks with elevated heat stress. An increasing likelihood of precipitation extremes in response to increasing humid heatwave amplitude in most of the sites in the subtropical region could be a consequence of recent

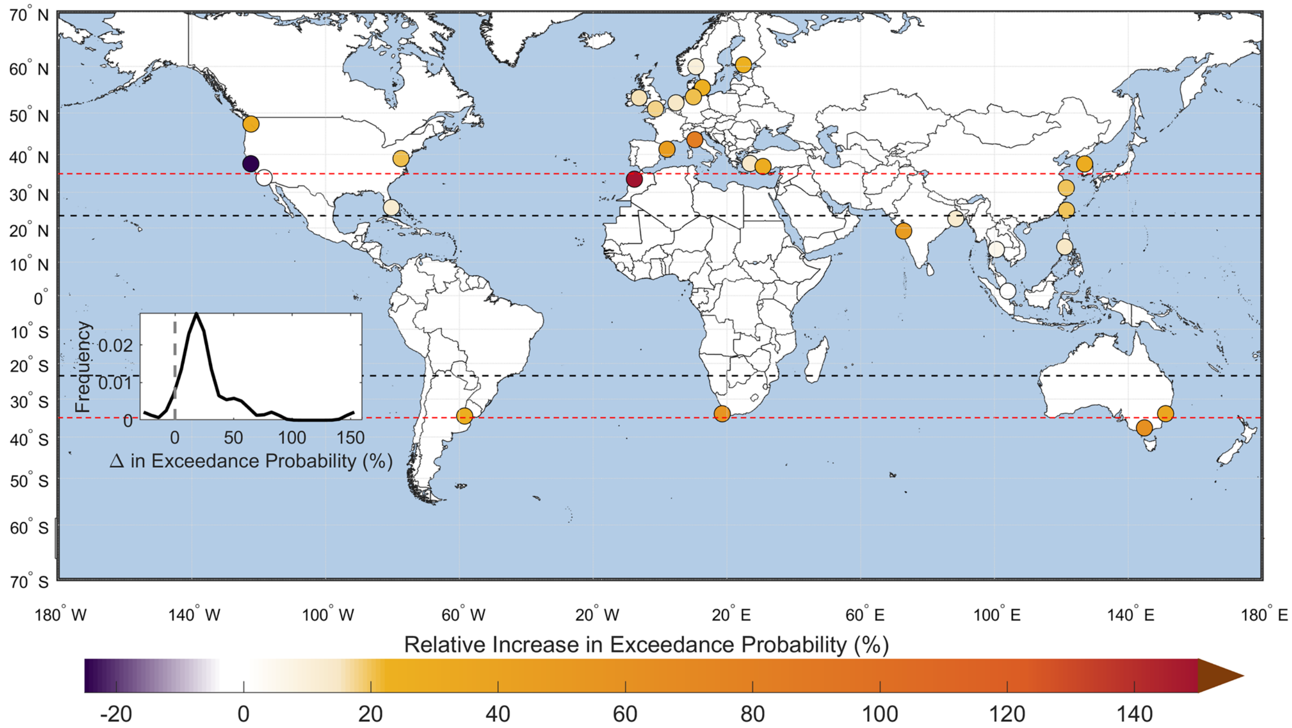

Fig. 9 | Relative change in exceedance probability of extreme rainfall with an increase of heatwave amplitude from its median to the 90th percentile. The relative change in exceedance probability (Δ) is determined using $\frac{P_2-P_1}{P_1}\times 100$, where $P_2 = P(P_{90}>p_{90}|H_D>h_{d\{90^{th}\}})$ and $P_1 = P(P_{90}>p_{90}|H_D>h_{d\{50^{th}\}})$. The arrow at the right end denotes that the relative change in exceedance probability lies beyond the 150% range. The inset shows the density function of relative changes in exceedance probability (in %) across sites.

shifts in subtropical highs, i.e., semi-permanent high-pressure systems (anticyclone) over the subtropical oceans during the summer in recent years, resulting in a higher temperature contrast of land vs ocean, and regionally-enhanced summer rainfall when it moves close to continents[62]. In the temperate climate regions, the increasing likelihood of extreme rainfall with increasing humid heatwave amplitude could be due to larger moisture availability in this region as compared to other climate regions[22].

We find significant delays in the mean timing of humid heatwaves at 52% (15 out of 29) of the megacities, while changes in the timing of extreme precipitation are small. This is in agreement with an earlier assessment[63] that reported shifts in timing of extreme precipitation by only a few days for most regions across the globe. 68% of sites show a significant shift in the timing of extreme precipitation, with smaller changes compared to the changes in the timing of temperature. Sites in Africa show larger shifts, with ranges between −0.10 and 0.09 days/decade. Further, changes in the mean response time between heatwave and the following extreme rainfall are also rather small. Four out of 29 stations show a significant decrease in response time, including the sites at the eastern coasts of North and South America. Our analyses show that in the northern hemisphere, ~25% (269 out of 1056) of the hot–wet compound events are characterized by moderate to super-extreme humid heatwaves followed by >1 − SD rainfall; among these, the tropics contribute the most (~50% of the events), whereas the subtropics contribute the least (~17%). Overall, sites across the southern hemisphere show a higher (4.2–5.7%) summer precursor coincidence rate, with the highest coincidence rate observed in the Melbourne and Buenos Aires areas. All four southern hemisphere gauges are located within a 20 km radius of the coast. The intensification of rainfall extremes across rapidly developing coastal megacities is influenced by the increased urbanization mediating the land–sea contrast of the coasts, by the urban heat island effect and ocean warming, and by changes in synoptic circulations, for example, the monsoon and Boreal Summer Intra-seasonal Oscillation[6,64–66]. However, previous assessments[64–66] have solely focused on mean and extreme precipitation events and their intra-seasonal variability, and have not considered the interactions between humid heat and extreme rainfall.

One possible mechanism for the heatwave peak intensity in the Pacific Northwest of North America is the strengthening and development of an atmospheric blocking high (a large, slow-moving high-pressure system), due to an increase in atmospheric water vapor content due to climate change[67,68]. In summer, heatwaves form primarily due to blocking-induced large-scale subsidence, leading to cloud-free skies and persistent radiative warming of the ground[69,70]. Further, Mo et al. [71] suggested that an increase in atmospheric water vapor content is linked with upstream atmospheric rivers, ahead of extreme heatwaves in the Pacific Northwest US, resulting in more persistent and severe heatwaves. The convergence of a strong high-pressure ridge and a warm-season landfalling atmospheric river, which induces moisture and heat transport, can affect the inland heat dome development during the summer. Further, delayed shifts in the timing of heatwave peak intensity and precipitation extremes in Southeast Australia are consistent with an earlier assessment[72]. Furthermore, the shift in the timing of humid heat conditions during the late-monsoon season in South Asia is often linked with monsoon breaks, including the delayed arrival of monsoon[47]. Recently, Dong et al. [73] showed that globally, over the northern hemisphere, compared with the reference period 1981–2000, the average change to delayed termination of heatwaves (up to +14 days) during 2001–2020 was about twice the average change to earlier onset (up to −7 days). The assessment of Dong et al. [73] showed that over the northern hemisphere, about 75% of sites show delayed mean termination of heatwaves; of this, about 39% of sites showed both delayed average onset and termination days of humid heatwaves. While the assessment of Dong et al. [73] exclusively covers gauges across the northern hemisphere, their findings support our insight into delayed shifts in the timing of humid heatwave peaks over the northern hemisphere. Further, analyzing a century (1925–2016) record, Oliver et al. [74] have shown that there has been an increase in global average marine heatwave frequency and duration, resulting in an over 50% increase in annual marine heatwave days globally. An increase in the intensity and duration of marine heatwaves also affects the intensity, persistence, and timing of summer heatwaves in coastal megacities[8,75]. This increases the likelihood of moisture-laden heatwaves with reduced wind speeds, particularly in high-latitude coastal regions[8].

In tropical regions, while extreme precipitation primarily occurs during monsoon seasons, the monsoon-dominated regimes are experiencing an expansion with intensification of rains and a prolonged monsoon season. In contrast, sites close to mid-latitude (for example, Alexandria) often experience an earlier shift in the timing of precipitation extreme[76]. This seasonal shift is possibly attributed to the increased frequency of southern-circulation weather types during spring[76]. On the other hand, a delayed shift in the timing of extreme precipitation is likely linked to the shift in large-scale atmospheric circulations, as observed in earlier assessments[72,77] from both hemispheres. Shifts in the North Atlantic Oscillation (NAO) since the 1980s may have resulted in the delayed arrival of extreme precipitation in the Northern hemisphere mid-latitude, especially over northwestern Europe[78]. The shift in the NAO pattern could possibly be due to polar warming[79]. The mean timing of warm-wet compound events (Fig. 5) closely follows the timing of their causal drivers, the individual climate stressors, heatwaves, and extreme precipitation (Figs. 3 and S1), which explains the early onset or delay in the timing of hot–wet compound events.

Since previous studies have primarily used reanalysis-based meteorological records or precipitation records of varying temporal resolutions to analyze hot–wet compound events at a global and continental scale, a direct comparison of these studies with our study may not be possible. Further, none of these assessments exclusively focus on coasts but report results on a continental scale. A qualitative comparison of these studies with ours shows an agreement and disparities in the following fronts: (1) Both You et al. [36] and Sauter et al. [46], and our study reveal that the northeastern United States shows a higher likelihood of extreme rainfall following heatwaves with a summer precursor coincidence rate of over 4.3% and an average frequency of over 1.6 events/year, whereas western coasts of the US show lower likelihood with precursor coincidence rates of 3.1–3.6% and an average frequency of less than an one event/year. In contrast to previous assessments, we also find a shorter response time from heatwave to extreme rainfall of <3 days, which shows a statistically significant decreasing trend across this region. While an increase in peak heatwave amplitude from the 50th to 90th percentile results in about a 12–20% increase in exceedance probability of extreme rainfall for the northeast US gauges, an increase in heatwave amplitude for the western US leads to no changes in extreme precipitation for Los Angeles and even 27% decline in extreme precipitation for San Francisco coast. In the western coast of the US, while hot summer drives aridity by increasing evaporative demand, the onset of the rainy season in this area is sometime during October–December[80], with a mean peak timing during January–February (Fig. 2). The asynchronicity between the timings of heatwave amplitude and peak precipitation leads to a decline in extreme precipitation likelihood following the heatwaves for the western coast of the US. (2) Both Sauter et al. [15,46] and our assessment show an increased likelihood of extreme rainfall following a heatwave on the southeastern coast of Australia. Further, we find a high summer precursor coincidence rate of ≥4.5% across these sites. (3) For the tropics, although we find a higher frequency of hot–wet compound events in Southeast Asia than in South Asia, overall, we find no significant increase (limited to ≤30%) in the likelihood of extreme precipitation in response to increased heatwave intensity. Our finding of no significant increase corroborates with Sauter et al.[46], which could be explained by the fact that the air is substantially less enriched with moisture during heatwaves, making it less conducive for hot–wet compound events in the tropics. Further, (4) Our finding of a lower likelihood of increase in extreme rainfall exceedance (around 12%) following moderate to high-intensity heatwaves on the East coast, compared to the West coast (approximately 47%), agrees with Sauter et al. [46]. However, in contrast to Sauter et al. [46], we find a higher summer precursor coincidence rate between humid heatwaves and precipitation extremes on the eastern coast of India (>3%) compared to the western coast (2.6%). This may be due to the development of intense marine heatwaves in the northern Bay of Bengal (≥15° N latitude) bordering the eastern coastal plains of India from June to September[81]. This may affect the development of humid heatwaves over land by drawing moisture from the ocean[8] and resulting in temperature-driven convective precipitation following an intense heatwave[82].

While station-based observations are often limited by the homogeneity and continuity of the records, and biases due to observational procedures, relocations, and changes in instrumentation types, their primary strength is their ability to precisely capture the local climatic, topographic, and land-use effects that may mediate extremes[45]. On the other hand, re-analysis and climate model-based datasets provide complete, consistent, and long-term time series, although they often under/overestimate extremes[38–41]. Most of the present-generation Earth system models, including global storm-resolving models, cannot adequately capture fine-scale climatic features near the coasts, such as the representation of humidity that controls the severity of humid heat stress[83,84]. Formal hypothesis-based research, combining different observational products, reanalysis, and climate-model simulations, could improve our understanding of the generation and changes of hot–wet compound events and the role of influencing factors such as the urban footprint. We hope that the derived insights can support climate model evaluations and provide a better understanding of the physical mechanisms linking heatwaves to extreme rainfall, which can aid in improved representations of atmospheric moisture and humidity terms in model parameterizations such that models can capture the complex interactions of hot–wet compound events and their dependence strengths[12,85]. This would provide valuable information for climate adaptation policies[86].

A few assessments[87–90] have shown an increasing likelihood of temporally compound tropical cyclones across the coasts of the eastern US and Southeast Asia[87,88], which can possibly exacerbate the frequency of hot–wet compound hazards by altering severe to exceptional heatwave characteristics and the preceding storm cyclogenesis[89,91], potentially impacting their compound interactions. The hydro-climatology of coastal megacities is complex due to interactions between land and marine heatwaves[8], teleconnection patterns[81], land–sea thermal contrasts[92], concurrent heatwaves and the following or preceding tropical cyclone-induced low-pressure genesis[87,89,91], dynamic interactions between near-shore salinity anomalies and marine heatwaves[93], city shape, density and height of buildings, and orographic orientation[6,94], all of which can impact the singular and the hot–wet compound events. However, understanding the effects of these physical mechanisms on hot–wet compound events is beyond the scope of this study. Future research should focus on identifying the role of drivers in changing the occurrence frequency and severity of hot–wet compound events and understanding the relative contributions of urbanization and climate change to changing characteristics across different climates and regions.

Methods

Analysis period and domain

Our analysis considers the boreal (March–September)[95] and austral[96,97] (November–February) summer during 1951–2022 for the three climate regions[98]: Tropics (23.5° N–23.5° S), subtropics (23.5° N–35° N and 23.5° S–35° S), and mid-latitudes (35° N–60° N and 35° S–60° S). Over the northern hemisphere, summer varies from March to September. In South Asia, heatwaves typically occur from March to June (Table S1 in Justin et al. [99]) with the highest mortality count observed from May to June. Heatwaves in northern Africa are primarily clustered from March to May, with occasional extremes in September[100,101]. In the Persian Gulf and South Asia, the wet-bulb temperature, the integrated measure of heat and humidity together, is consistently high during May–June and July–August[99,102]. In Europe, persistent heatwaves are observed during June to September[103,104], while in the US, heatwaves are mostly confined to June–July[103,105]. In contrast, the austral summer spans from November to February[106,107], with peak heatwaves during December–February[108,109]. Initially, we selected 34 cities within a 100 km radius of the coastline (Table S1) with a minimum distance to the coast of ~2.0 km (Manilla in the Philippines) and a maximum distance of ~75 km (Washington Dulls International airport, Washington DC in the United States), spatially distributed across all three climate regions.

Observation-derived records

We analyze hot–wet compound events during summer seasons over global coastal megacities that are located within a 100 km radius of the coast[110] and are the center of major economic (trade and finance, marine transportation) activities, tourism industries, and recreation (Table S1). Our choice of the cities is motivated by earlier studies[8,110] and further modified based on the availability of quality-controlled, high-resolution meteorological records and their population size. Of the cities analyzed, 69% belong to large metropolitan areas with a population of >1.5 M, 24—metropolitan areas with a population between 0.5 M and 1.5 M, whereas only 7% belong to small urban areas with a population < 0.2 M[111]. The selection of sites is not uniform globally due to data availability. Those megacities are selected within a 100 km radius distance from the coast for which quality-controlled sub-daily meteorological records are available, such as dry-bulb, dew point temperature, sea-level pressure, and daily precipitation. Although a few studies have used quality-controlled station-based records[75] or high-resolution gridded observations[112,113], they have considered daily maximum air temperature and do not analyze humid heat, which has more serious consequences for living organisms than dry heat alone[114–116]. Further, the primary components of humid heat metrics, surface air temperature, and especially humidity series, often suffer from inhomogeneities in station-based records; in several cases, they are unavailable. Following earlier studies[8,38], we examine humid heat stress using station-based sub-daily (ranges from 1- to 3-hourly) HadISD (Hadley Centre Integrated Surface Database) observational time series[117] for the period 1951–2022. HadISD is a station-based product providing quality-controlled, homogeneous, high-resolution (hourly, 3-hourly) records of near-surface air temperature (2-m height), dewpoint temperature, sea-level pressure, and precipitation. Several checks are implemented to discard stations with excessive and obvious typographical or instrumental errors, as well as individual occurrences of these issues. However, precipitation in HadISD observations is not quality controlled. HadISD has been widely used in analyzing humid heat stress globally[38,102,116,118]. We sampled sub-daily time series of dry-bulb temperature (DBT), dew-point temperature, and mean sea-level pressure and topographic information, such as elevation. Following Raymond et al. [38], we performed detailed climatological and meteorological tests to screen the hydrometric data. The selected megacities provide the best available quality-controlled at-site records and have been used in earlier assessments[8,110].

We obtained station-based daily precipitation time series from two quality-controlled, global-scale in-situ observational networks: (i) Global Surface Summary of the Day (GSOD) dataset archived at NOAA's National Climate Data Centre[119] (ii) Global Historical Climatology Network-daily (GHCN-d)[120]. GHCN-d observations have a sensitivity of 0.1 mm and undergo a series of quality checks[121]. GSOD offers automated quality-controlled data products, where random errors are removed and corrections are implemented to account for changes in instrumentation, station relocation, and changes in time of observations[122]. These datasets have been extensively used to analyze extreme precipitation in regional-scale[123,124] and global-scale studies[122]. After carefully investigating both sources, we selected for each site a long and reasonably complete, quality-controlled daily precipitation time series from either GSOD or GHCN-d, depending on the quality and length of the observed series (see Table S1). The temperature and precipitation observational networks are situated within a 25 km radius with a median radius of 1.9 km (Table S1). The population data for cities for 2020 were retrieved from the World Urbanization Prospects: The 2018 Revision[125].

Identification of singular and compound events

We use the Davies-Jones method[126,127] and a revised MATLAB-based implementation[128] following the corrections indicated in ref. 129, to determine sub-daily wet-bulb temperature. Following Russo et al. [130], a humid heatwave episode is identified as a period of at least three consecutive days when the daily maximum wet-bulb temperature, HW_d, exceeds a daily percentile-based variable threshold. As a threshold, we use the 90th percentile of HW_d smoothed with a 31-day moving average filter[131] throughout the summer season. Since the daily threshold time series appears to be a jagged curve, resulting in several short-duration heatwave episodes, following the literature[104,131], a centered moving average of 31 days (i.e., ±15-day) was applied as a smoothing filter. The peak intensity, i.e., the amplitude of a heatwave episode (h_d), is the hottest day of a humid heatwave[132]. To assess the severity of a humid heatwave event, we determine the accumulated daily Humid Heatwave Magnitude Index[59] ($AHWMI_d$), defined as the sum of the daily humid heatwave magnitude, $HWMI_d$ (described in Eq. 1) over the duration of a heatwave episode. It thus accounts for the severity of temperature anomalies exceeding a certain normalized threshold throughout the duration of the heatwave episode[59]. The $HWMI_d$ during the d-day heatwave episode is defined as follows:

$$AHWMI_d = \sum_{d=1}^{n} HWMI_d,\ d \in [3, n] \tag{1}$$

Where, $HWMI_d = \begin{cases} \frac{HW_d - HW_{25p}}{HW_{75p} - HW_{25p}}\ if\ HW_d > HW_{25p} \\ 0\ if\ HW_d < HW_{25p} \end{cases}$

HW_{25p} and HW_{75p} are the 25th and 75th percentile values of HW_d values during the summer months of the analysis period. $AHWMI_d$ values are used to classify heatwave conditions: normal or no heatwave conditions (0–5), moderate (>5–10), severe (>10–15), extreme (>15–30), very extreme (>30–50), and super extreme (>50–80) conditions[59].

A daily precipitation extreme (p_{90}) for a site is defined if the daily precipitation magnitude exceeds the 90th percentile of all wet days during the analysis period[133]. A hot–wet compound event is identified when the peak intensity of a humid heatwave precedes the daily precipitation extreme within a window of $t \epsilon [-1, 7]$ days. The response time of the event is defined as the duration between the day of the heatwave peak and the day of the precipitation extreme within the $t \epsilon [-1, 7]$ days window. Since the warmest day of a heatwave may not necessarily occur on the first day of the event, a time window of $t \in [-1, 7]$ days was selected to sample the peak heatwave intensity and the following p_{90} event. Although extreme rainfall following the summertime heatwaves is caused by localized convection, it may not occur on the next day. Hence, a time window is required to consider this lagged effect[36,134,135]. The precipitation can attain its maximum peak during the initial development phase of a heatwave episode. A lagged response between high temperatures and storms may stem from atmospheric circulation, shifts in the synoptic environment, and land–sea atmospheric feedback[23,61]. Further, a heatwave often follows a slow-moving tropical cyclone. An elevated air temperature within a week of the tropical cyclone landfall is caused by changes in the atmospheric circulation because of the development of an anticyclonic pattern, resulting in warm air subsidence, leading to a heatwave episode[136,137]. A comparison of lag times (Fig. S3) shows positive lagged responses for 83% (971 out of 1166 event pairs) of compound occurrences and 10% (111 out of 1166 event pairs) occurrences on the same day, implying either p_{90} events follow (or precedes) heatwave amplitudes on the same day with a time lag of a few hours. Only 7% (84 out of 1166 event pairs) of p_{90} events precede heatwave amplitude, indicating they are possibly tropical cyclone-heatwave compounded events. Following refs. 138,139 single and compound events are separated by at least three days to be identified as independent events. To ensure adequate sample lengths to investigate trends in the occurrence of hot–wet compound events, we consider only sites with at least ten hot–wet compound events. According to this criterion, 29 out of 34 sites were finally retained, with the total number of hot–wet compound events varying from 12 to 122 during the analysis period.

Further, we investigate the dependence strength in the tails of compound extremes using the non-parametric Capéraà–Fougères–Genest upper tail correlations[140]. The statistical significance of the upper tail correlation is determined by drawing $N = 10{,}000$ random bootstrap samples and then computing the P-value (i.e., the probability of observing a stronger dependence strength by chance) from the simulated bootstrap samples using the typical percentile-based approach. To increase the power of the statistical test, we report the statistical significance at the 10% significance level.

Analyzing changes in the seasonality of singular and compound extreme events

We employ directional statistics to analyze changes in the seasonality (or timing) of single climate stressors, heatwaves, and extreme precipitation events[72,141]. We use two seasonality indices, i.e., the weighted mean occurrence day and its circular variability that quantify the average event timing and the variability in the timing, respectively[142]. For n events, the weighted mean occurrence day of singular climate stressors is determined using the following equations[143]

$$\bar{x}_\delta = \frac{\sum_{i=1}^{n} h_{d_i} \cdot \cos\delta_i}{\sum_{i=1}^{n} h_{d_i}}; \bar{y}_\delta = \frac{\sum_{i=1}^{n} h_{d_i} \cdot \sin\delta_i}{\sum_{i=1}^{n} h_{d_i}} \tag{2a}$$

$$\bar{x}_\delta = \frac{\sum_{i=1}^{n} p_{90} \cdot \cos\delta_i}{\sum_{i=1}^{n} p_{90}}; \bar{y}_\delta = \frac{\sum_{i=1}^{n} p_{90} \cdot \sin\delta_i}{\sum_{i=1}^{n} p_{90}} \tag{2b}$$

Following the literature[77], the mean occurrence day of the compound events is determined using the simple circular mean of the individual climate stressors.

Where, $\delta_i = J_i \frac{2\pi}{l}$, J indicates Julian dates ranging from 1 to 365 for regular years, and 1 to 366 for leap years, l is the number of days in a calendar year, and m indicates the observed events.

The mean directional angle is determined by refs. 143,77

$$\bar{\delta} = \begin{cases} \tan^{-1}\left(\frac{\bar{y}_\delta}{\bar{x}_\delta}\right) \; if \; \bar{x}_\delta > 0 \; and \; \bar{y}_\delta > 0 \\ 180 - \tan^{-1}\left(\frac{\bar{y}_\delta}{\bar{x}_\delta}\right) \; if \; \bar{x}_\delta < 0 \; and \; \bar{y}_\delta > 0 \\ 180 + \tan^{-1}\left(\frac{\bar{y}_\delta}{\bar{x}_\delta}\right) \; if \; \bar{x}_\delta < 0 \; and \; \bar{y}_\delta < 0 \\ 360 + \tan^{-1}\left(\frac{\bar{y}_\delta}{\bar{x}_\delta}\right) \; if \; \bar{x}_\delta > 0 \; and \; \bar{y}_\delta < 0 \\ \pi/2 \; if \; \bar{x}_\delta = 0 \; and \; \bar{y}_\delta > 0 \\ 3\pi/2 \; if \; \bar{x}_\delta = 0 \; and \; \bar{y}_\delta < 0 \end{cases} \tag{3}$$

$$\text{The weighted mean occurrence day is } WMOD = \bar{\delta} \times \left(\frac{\bar{l}}{2\pi}\right) \tag{4}$$

Where, $\bar{l}$ denotes the average number of days in, a year, considering the number of days in leap and non-leap years. The variability in the event timing is determined using circular variance, $\sigma^2 = -2\log(\bar{W}_p)$, where $\bar{W}_p = \sqrt{\bar{x}_\delta^{\,2} + \bar{y}_\delta^{\,2}}$.

Trends in the timing of heatwave amplitude and daily extreme precipitation are investigated using the nonparametric adjusted Theil-Sen estimator for slope, β, which is the median of the difference in event dates over all possible combinations of time stamps (i and j) within the time series[77]

$$\beta = median\left[\frac{J_j - J_i + \gamma}{j - i}\right], \text{ where } \gamma = \begin{cases} -\bar{l} \; if \; (J_j - J_i) > \bar{l}/2 \\ \bar{l} \; if \; (J_j - J_i) < \bar{l}/2 \\ 0, \; otherwise \end{cases} \tag{5}$$

We evaluate trend significance via a resampling-based approach with $N = 2000$ bootstrap runs[144]. Significance of trends is reported at P-value < 0.05 for earlier onset (negative trend) and P-value > 0.95 for delayed arrival (positive trend) of events.

Analyzing precursor coincidence rates of hot–wet compound events

For analyzing response (i.e., coincidence) rates between the drivers of hot–wet compound events, we employ event coincidence analysis (ECA), which tests for the sequential occurrence of humid heatwaves preceding extreme precipitation. We analyze response rates between heatwave amplitudes at times $t_i^{h_d,k} (i = 1, \ldots., \mathrm{N_{h_d,k}})$ and precipitation extremes $t_j^{p,k}(\varepsilon)(j = 1, \ldots., \mathrm{N_{p,k}}(\varepsilon))$ within a coincidence interval $\Delta T = 7$-day. For a given site k, $N_{h_d,k}$ and $N_{p,k}(\varepsilon)$ indicate the counts of humid heatwaves and precipitation extremes during summers in both hemispheres. We obtain the precursor coincidence rate $r_p(\Delta T, \varepsilon)$, which represents the fraction of humid heatwave amplitudes that are preceding p_{90} events, i.e., precipitation magnitude that exceeds the ε threshold and has occurred within the ΔT time window during the summer season[145]:

$$r_p(\Delta T, \varepsilon) = \frac{1}{N_{p,k}(\varepsilon)} \sum_{i=1}^{N_{h_{d,k}}} \phi\left[\sum_{j=1}^{N_{p,k(\varepsilon)}} I_{\{0,\Delta T\}}\left(t_j^{p,k}(\varepsilon) - t_i^{h_{d,k}}\right)\right] \tag{6}$$
$$i = 1, \ldots., N_{h_d,k}; \; j = 1, \ldots., N_{p,k}(\varepsilon); \; r_p \in (0, 1)$$

$\phi(.)$ indicates the heavy side function $\phi(x) = 0$ for $x \le 0$ and $\phi(x) = 1$, otherwise. $I(.)$ is the indicator function with $I(x) = 1$ for $x \in (0, \Delta T)$ or 0 otherwise. Values of r_p close to 0 indicate that the two drivers do not coincide, while values close to 1 show that most h_d events precede a p_{90} event. We evaluate the statistical significance of event coincidence using a bootstrap-based approach with $N = 10{,}000$ bootstrap runs at a 5% significance level.

Conditional bivariate model

We determine the relative changes in exceedance probability of extreme rainfall (p_{90}) events, preconditioned on humid heat stress, when the heatwave amplitude, h_d increases from its median value to the 90th percentile for a given site, using a copula-based conditional probability approach[146]: $P(P_{90} > p_{90} | H_D > h_{d\{90th\}}) - P(P_{90} > p_{90} | H_D > h_{d\{50th\}})$. The copula-based joint probability distribution of p_{90} and h_d reads as follows

$$F_{P_{90}H_I}(p_{90}, h_d) = C[F_{P_{90}}(p_{90}), F_{H_D}(h_d)] \tag{7}$$

Where $C(.)$ is the cumulative distribution function (CDF) of the bivariate copula function with marginal CDFs of peak humid heatwave intensity, $F_{H_D}(h_d)$ and heatwave preconditioned precipitation extreme, $F_{P_{90}}(p_{90})$, respectively. Copulas represent multivariate distribution functions using univariate probability distributions (i.e., marginal CDFs) of any form and serve as a mapping tool from the variable space to the sample space that is uniformly distributed in [0,1]. Copulas are a powerful tool to model the dependence of random vectors. The conditional likelihood of $P(P_{90} > p_{90} | H_D > h_{d\{50^{th}\}})$ is given as follows[146]

$$P(P_{90} > p_{90} | H_D > h_{d\{50^{th}\}}) = \frac{1 - F_{P_{90}}(p_{90}) - F_{H_D}(h_d) + C[F_{P_{90}}(p_{90}), F_{H_D}(h_d)]}{1 - F_{H_D}(h_d)} \tag{8}$$

We consider a wide range of bivariate copula families, namely the Clayton, (flipped) rotatory Clayton, Frank, Gumbel-Hougaard, Plackett, and Student's t copulas for modeling dependence between the two drivers, h_d and p_{90}. We use the maximum pseudo-likelihood method to estimate the parameters of the copula family[147]. Following ref. 148, the copula families are selected based on the maximum P-values (Table S2 and Fig. S4), which is based on the Crámer-von Mises type goodness-of-fit test[149] that compares the empirical (C_{emp}) vs the parametric copula (C_θ) probabilities through $\sqrt{n}(C_{emp} - C_\theta)$, where n is the number of compound events. For modeling the marginal distributions of the drivers, we consider commonly used univariate probability distributions, namely the gamma, log-normal, generalized extreme value (GEV), log-logistic, and Weibull distributions. We select the best-fitted univariate probability distribution based on the minimum Akaike information criterion (AIC) with small sample correction[150], while we evaluate the goodness-of-fit of the selected distributions using the Kolmogorov-Smirnov goodness-of-fit test (Tables S3 and S4; and Figs. S5 and S6).

Data availability

Station-based sub-daily (ranges from 1- to 3-hourly) HadISD observational time series is obtained from the Met Office Hadley Centre Observations repository: https://www.metoffice.gov.uk/hadobs/hadisd/v341_202402p/download.html, daily precipitation time series are obtained from (1) Global Surface Summary of the Day (GSOD) dataset archived at NOAA's National Climate Data Centre available at: https://www.ncei.noaa.gov/access/search/data-search/global-summary-of-the-day (2) Global Historical Climatology Network-daily (GHCN-d) available at: https://www.ncei.noaa.gov/data/global-historical-climatology-network-daily/access/. The population data for urban agglomerations is publicly available at: https://population.un.org/wup/Download/.

Code availability

Computer codes used in this study can be made available from the corresponding author upon request.

Received: 25 September 2024; Accepted: 25 March 2025;

References

1. Duedall, I. W. & Maul, G. A. Demography of coastal populations. *Encycl. Coast. Sci. Encycl. Earth Sci. Ser.* **368**, 374 (2005).
2. Feng, K., Ouyang, M. & Lin, N. Tropical cyclone-blackout-heatwave compound hazard resilience in a changing climate. *Nat. Commun.* **13**, 4421 (2022).
3. Tay, C. et al. Sea-level rise from land subsidence in major coastal cities. *Nat. Sustain* **5**, 1049–1057 (2022).
4. Bevacqua, E. et al. More meteorological events that drive compound coastal flooding are projected under climate change. *Commun. Earth Environ.* **1**, 1–11 (2020).
5. Zhang, H. et al. Unequal urban heat burdens impede climate justice and equity goals. *Innovation* **4**, 100488 (2023).
6. Xiao, Y. et al. Weakened sea-land breeze in a coastal megacity driven by urbanization and ocean warming. *Earth's Future* **11**, e2022EF003341 (2023).
7. Luo, M. et al. Anthropogenic forcing has increased the risk of longer-traveling and slower-moving large contiguous heatwaves. *Sci. Adv.* **10**, eadl1598 (2024).
8. Hu, L. A Global assessment of coastal marine heatwaves and their relation with coastal urban thermal changes. *Geophys. Res. Lett.* **48**, e2021GL093260 (2021).
9. Curtis, S. Means and long-term trends of global coastal zone precipitation. *Sci. Rep.* **9**, 5401 (2019).
10. Stone, B. Jr. et al. How blackouts during heat waves amplify mortality and morbidity risk. *Environ. Sci. Technol.* **57**, 8245–8255 (2023).
11. Hatsuzuka, D., Sato, T. & Higuchi, Y. Sharp rises in large-scale, long-duration precipitation extremes with higher temperatures over Japan. *npj Clim. Atmos. Sci.* **4**, 29 (2021).
12. Zscheischler, J. & Seneviratne, S. I. Dependence of drivers affects risks associated with compound events. *Sci. Adv.* **3**, e1700263 (2017).
13. Trenberth, K. E. & Shea, D. J. Relationships between precipitation and surface temperature. *Geophys. Res. Lett.* **32**, L14703 (2005).
14. Ganguli, P. & Merz, B. Observational evidence reveals compound humid heat stress-extreme rainfall hotspots in India. *Earth's Future* **12**, e2023EF004074 (2024).
15. Sauter, C., Catto, J. L., Fowler, H. J., Westra, S. & White, C. J. Compounding heatwave-extreme rainfall events driven by fronts, high moisture, and atmospheric instability. *J. Geophys. Res. Atmos.* **128**, e2023JD038761 (2023).
16. You, J. & Wang, S. Higher probability of occurrence of hotter and shorter heat waves followed by heavy rainfall. *Geophys. Res. Lett.* **48**, e2021GL094831 (2021).
17. Chen, Y., Liao, Z., Shi, Y., Tian, Y. & Zhai, P. Detectable increases in sequential flood-heatwave events across China during 1961–2018. *Geophys. Res. Lett.* **48**, e2021GL092549 (2021).
18. Liu, J. et al. Understanding compound extreme precipitations preconditioned by heatwaves over China under climate change. *Environ. Res. Lett.* **19**, 064077 (2024).
19. Li, C. et al. Urbanization-induced increases in heavy precipitation are magnified by moist heatwaves in an urban agglomeration of East China. *J. Clim.* **36**, 693–709 (2023).
20. Chen, Y., Liao, Z., Shi, Y., Li, P. & Zhai, P. Greater flash flood risks from hourly precipitation extremes preconditioned by heatwaves in the Yangtze River Valley. *Geophys. Res. Lett.* **49**, e2022GL099485 (2022).
21. Liu, X. et al. Spatially distinct effects of preceding precipitation on heat stress over eastern China. *Environ. Res. Lett.* **12**, 115010 (2017).
22. Sauter, C., White, C. J., Fowler, H. J. & Westra, S. Temporally compounding heatwave–heavy rainfall events in Australia. *Int. J. Climatol.* **43**, 1050–1061 (2023).
23. Zhang, W. & Villarini, G. Deadly compound heat stress-flooding hazard across the central United States. *Geophys. Res. Lett.* **47**, e2020GL089185 (2020).
24. Gu, L. et al. Global increases in compound flood-hot extreme hazards under climate warming. *Geophys. Res. Lett.* **49**, e2022GL097726 (2022).
25. Chiang, F., Greve, P., Mazdiyasni, O., Wada, Y. & AghaKouchak, A. A Multivariate conditional probability ratio framework for the detection and attribution of compound climate extremes. *Geophys. Res. Lett.* **48**, e2021GL094361 (2021).
26. Zhou, Z. et al. Global increase in future compound heat stress-heavy precipitation hazards and associated socio-ecosystem risks. *npj Clim. Atmos. Sci.* **7**, 1–14 (2024).
27. Markonis, Y. et al. The rise of compound warm-season droughts in Europe. *Sci. Adv.* **7**, eabb9668 (2021).
28. Peng, T. et al. Changes in temperature-precipitation compound extreme events in China during the past 119 years. *Earth Space Sci.* **10**, e2022EA002777 (2023).
29. Dash, S. & Maity, R. Revealing alarming changes in spatial coverage of joint hot and wet extremes across India. *Sci. Rep.* **11**, 18031 (2021).
30. De Luca, P., Messori, G., Faranda, D., Ward, P. J. & Coumou, D. Compound warm–dry and cold–wet events over the Mediterranean. *Earth Syst. Dyn.* **11**, 793–805 (2020).
31. Xoplaki, E. et al. Compound events in Germany in 2018: drivers and case studies. *Nat. Hazards Earth Syst. Sci.* **25**, 541–564 (2025).
32. Bevacqua, E. et al. Advancing research on compound weather and climate events via large ensemble model simulations. *Nat. Commun.* **14**, 2145 (2023).
33. Tabari, H. & Willems, P. Global risk assessment of compound hot–dry events in the context of future climate change and socioeconomic factors. *NPJ Clim. Atmos. Sci.* **6**, 74 (2023).
34. Meng, Y., Hao, Z., Feng, S., Zhang, X. & Hao, F. Increase in compound dry-warm and wet-warm events under global warming in CMIP6 models. *Glob. Planet. Change* **210**, 103773 (2022).
35. Vogel, M. M., Hauser, M. & Seneviratne, S. I. Projected changes in hot, dry and wet extreme events' clusters in CMIP6 multi-model ensemble. *Environ. Res. Lett.* **15**, 094021 (2020).
36. You, J., Wang, S., Zhang, B., Raymond, C. & Matthews, T. Growing threats from swings between hot and wet extremes in a warmer world. *Geophys. Res. Lett.* **50**, e2023GL104075 (2023).

37. Wolf, K., Bellouin, N., Boucher, O., Rohs, S. & Li, Y. Correction of ERA5 temperature and relative humidity biases by bivariate quantile mapping for contrail formation analysis. *Atmos. Chem. Phys.* **25**, 157–181 (2025).
38. Raymond, C., Matthews, T. & Horton, R. M. The emergence of heat and humidity too severe for human tolerance. *Sci. Adv.* **6**, eaaw1838 (2020).
39. Freychet, N., Tett, S. F. B., Yan, Z. & Li, Z. Underestimated change of wet-bulb temperatures over East and South China. *Geophys. Res. Lett.* **47**, e2019GL086140 (2020).
40. Fallah, A., Rakhshandehroo, G. R., Berg, P., O, S. & Orth, R. Evaluation of precipitation datasets against local observations in southwestern Iran. *Int. J. Climatol.* **40**, 4102–4116 (2020).
41. Jiao, D., Xu, N., Yang, F. & Xu, K. Evaluation of spatial-temporal variation performance of ERA5 precipitation data in China. *Sci. Rep.* **11**, 17956 (2021).
42. He, L., Zhou, T. & Chen, X. South Asian summer rainfall from CMIP3 to CMIP6 models: biases and improvements. *Clim. Dyn.* **61**, 1049–1061 (2023).
43. Klutse, N. A. B. et al. The climatic analysis of summer monsoon extreme precipitation events over West Africa in CMIP6 simulations. *Earth Syst. Environ.* **5**, 25–41 (2021).
44. Tang, Z. et al. Future changes in the risk of compound hot and dry events over China estimated with two large ensembles. *PLoS One* **17**, e0264980 (2022).
45. Shreevastava, A., Raymond, C. & Hulley, G. C. Contrasting intraurban signatures of humid and dry heatwaves over Southern California. *J. Appl. Meteor. Climatol.* https://doi.org/10.1175/JAMC-D-22-0149.1 (2023).
46. Sauter, C. et al. Compound extreme hourly rainfall preconditioned by heatwaves most likely in the mid-latitudes. *Weather Clim. Extrem.* **40**, 100563 (2023).
47. Ivanovich, C. C., Horton, R. M., Sobel, A. H. & Singh, D. Subseasonal variability of humid heat during the south asian summer monsoon. *Geophys. Res. Lett.* **51**, e2023GL107382 (2024).
48. Saeed, F., Schleussner, C.-F. & Ashfaq, M. Deadly heat stress to become commonplace across South Asia already at 1.5°C of global warming. *Geophys. Res. Lett.* **48**, e2020GL091191 (2021).
49. Yaddanapudi, R., Mishra, A., Huang, W. & Chowdhary, H. Compound wind and precipitation extremes in global coastal regions under climate change. *Geophys. Res. Lett.* **49**, e2022GL098974 (2022).
50. Zhou, M. & Wang, S. The risk of concurrent heatwaves and extreme sea levels along the global coastline is increasing. *Commun. Earth Environ.* **5**, 1–10 (2024).
51. Lewis, E. et al. Quality control of a global hourly rainfall dataset. *Environ. Model. Softw.* **144**, 105169 (2021).
52. Aerts, J. C. J. H. et al. Evaluating flood resilience strategies for coastal megacities. *Science* **344**, 473–475 (2014).
53. Merz, B. et al. Causes, impacts and patterns of disastrous river floods. *Nat. Rev. Earth Environ.* **2**, 592–609 (2021).
54. Geen, R., Bordoni, S., Battisti, D. S. & Hui, K. Monsoons, ITCZs, and the concept of the global monsoon. *Rev. Geophys.* **58**, e2020RG000700 (2020).
55. Peel, M. C., Finlayson, B. L. & McMahon, T. A. Updated world map of the Köppen–Geiger climate classification. *Hydrol. Earth Syst. Sci.* **11**, 1633–1644 (2007).
56. Paltan, H. et al. Global floods and water availability driven by atmospheric rivers. *Geophys. Res. Lett.* **44**, 387–395 (2017).
57. Neiman, P. J. et al. Diagnosis of an intense atmospheric river impacting the Pacific Northwest: storm summary and offshore vertical structure observed with COSMIC satellite retrievals. *Monthly Weather Rev.* **136**, 4398–4420 (2008).
58. Reid, K. J., Rosier, S. M., Harrington, L. J., King, A. D. & Lane, T. P. Extreme rainfall in New Zealand and its association with Atmospheric Rivers. *Environ. Res. Lett.* **16**, 044012 (2021).
59. Zittis, G. et al. Business-as-usual will lead to super and ultra-extreme heatwaves in the Middle East and North Africa. *npj Clim. Atmos. Sci.* **4**, 1–9 (2021).
60. Fowler, H. J. et al. Anthropogenic intensification of short-duration rainfall extremes. *Nat. Rev. Earth Environ.* **2**, 107–122 (2021).
61. Raghavendra, A., Dai, A., Milrad, S. M. & Cloutier-Bisbee, S. R. Floridian heatwaves and extreme precipitation: future climate projections. *Clim. Dyn.* **52**, 495–508 (2019).
62. Li, W., Li, L., Ting, M. & Liu, Y. Intensification of Northern Hemisphere subtropical highs in a warming climate. *Nat. Geosci.* **5**, 830–834 (2012).
63. Gründemann, G. J., Zorzetto, E., Van De Giesen, N. & Van Der Ent, R. J. Historical shifts in seasonality and timing of extreme precipitation. *Geophys. Res. Lett.* **50**, e2023GL105200 (2023).
64. Yan, H. et al. Urbanization further intensifies short-duration rainfall extremes in a warmer climate. *Geophys. Res. Lett.* **51**, e2024GL108565 (2024).
65. Hunt, K. M. R., Turner, A. G., Stein, T. H. M., Fletcher, J. K. & Schiemann, R. K. H. Modes of coastal precipitation over southwest India and their relationship with intraseasonal variability. *Quart. J. R. Meteor. Soc.* **147**, 181–201 (2021).
66. Sreenath, A. V., Abhilash, S., Vijaykumar, P. & Mapes, B. E. West coast India's rainfall is becoming more convective. *npj Clim. Atmos. Sci.* **5**, 1–7 (2022).
67. White, R. H. et al. The unprecedented Pacific Northwest heatwave of June 2021. *Nat. Commun.* **14**, 727 (2023).
68. Zhang, X. et al. Increased impact of heat domes on 2021-like heat extremes in North America under global warming. *Nat. Commun.* **14**, 1690 (2023).
69. Kautz, L.-A. et al. Atmospheric blocking and weather extremes over the Euro-Atlantic sector— a review. *Weather Clim. Dyn.* **3**, 305–336 (2022).
70. Cai, F. et al. Sketching the spatial disparities in heatwave trends by changing atmospheric teleconnections in the Northern Hemisphere. *Nat. Commun.* **15**, 8012 (2024).
71. Mo, R., Lin, H. & Vitart, F. An anomalous warm-season trans-Pacific atmospheric river linked to the 2021 western North America heatwave. *Commun. Earth Environ.* **3**, 1–12 (2022).
72. Wasko, C., Nathan, R. & Peel, M. C. Changes in antecedent soil moisture modulate flood seasonality in a changing climate. *Water Resour. Res.* **56**, e2019WR026300 (2020).
73. Dong, J. et al. Trends of the intra-annual onset and end of humid heatwaves in the Northern Hemisphere. *Earth's Future* **12**, e2024EF005163 (2024).
74. Oliver, E. C. J. et al. Longer and more frequent marine heatwaves over the past century. *Nat. Commun.* **9**, 1324 (2018).
75. Risser, M. D., Zhang, L. & Wehner, M. F. Data-driven upper bounds and event attribution for unprecedented heatwaves. *Weather Clim. Extrem.* **47**, 100743 (2025).
76. Tramblay, Y. et al. Changes in Mediterranean flood processes and seasonality. *Hydrol. Earth Syst. Sci.* **27**, 2973–2987 (2023).
77. Blöschl et al. Changing climate shifts timing of European floods. *Science* **357**, 588–590 (2017).
78. Hurrell, J. W. & van Loon, H. Decadal variations in climate associated with the North Atlantic oscillation. *Climatic Change* **36**, 301–326 (1997).
79. Hanna, E., Cropper, T. E., Jones, P. D., Scaife, A. A. & Allan, R. Recent seasonal asymmetric changes in the NAO (a marked summer decline and increased winter variability) and associated changes in the AO and Greenland Blocking Index. *Int. J. Climatol.* **35**, 2540–2554 (2015).
80. Swain, D. L. et al. Increasing hydroclimatic whiplash can amplify wildfire risk in a warming climate. *Glob. Change Biol.* **31**, e70075 (2025).
81. Saranya, J. S., Roxy, M. K., Dasgupta, P. & Anand, A. Genesis and trends in marine heatwaves over the tropical indian ocean and their

interaction with the indian summer monsoon. *J. Geophys. Res. Oceans* **127**, e2021JC017427 (2022).

82. Dowdy, A. J. & Catto, J. L. Extreme weather caused by concurrent cyclone, front and thunderstorm occurrences. *Sci. Rep.* **7**, 40359 (2017).
83. Merlis, T. M. et al. Climate sensitivity and relative humidity changes in global storm-resolving model simulations of climate change. *Sci. Adv.* **10**, eadn5217 (2024).
84. Mooers, G. et al. Comparing storm resolving models and climates via unsupervised machine learning. *Sci. Rep.* **13**, 22365 (2023).
85. Lang, T. et al. Sources of uncertainty in mid-tropospheric tropical humidity in global storm-resolving simulations. *J. Adv. Model Earth Syst.* **15**, e2022MS003443 (2023).
86. Liang, C.-M. et al. Rapid increase in warm–wet compound extreme events with high health risks in southern China: Joint influence of ENSO and the Indian Ocean. *Adv. Clim. Change Res.* **14**, 856–865 (2023).
87. Wu, J. et al. Increasing risk from landfalling tropical cyclone-heatwave compound events to coastal and inland China. *Environ. Res. Lett.* **17**, 105007 (2022).
88. Chen, J. et al. Changing impacts of tropical cyclones on East and Southeast Asian inland regions in the past and a globally warmed future climate. *Front. Earth Sci.* **9**, 1065 (2021).
89. Matthews, T., Wilby, R. L. & Murphy, C. An emerging tropical cyclone-deadly heat compound hazard. *Nat. Clim. Change* **9**, 602–606 (2019).
90. Xi, D., Lin, N. & Gori, A. Increasing sequential tropical cyclone hazards along the US East and Gulf coasts. *Nat. Clim. Change* **13**, 258–265 (2023).
91. Guido, Z., Allen, T., Mason, S. & Méndez-Lázaro, P. Hurricanes and anomalous heat in the Caribbean. *Geophys. Res. Lett.* **49**, e2022GL099740 (2022).
92. Wehner, M., Stone, D., Krishnan, H., AchutaRao, K. & Castillo, F. The deadly combination of heat and humidity in India and Pakistan in Summer 2015. *Bull. Am. Meteorol. Soc.* **97**, S81–S86 (2016).
93. Sims, L. D., Subrahmanyam, B. & Trott, C. B. Influence and characteristics of anticyclonic eddies in active MHW years in the Northwest Atlantic. *Front. Mar. Sci*. https://doi.org/10.3389/fmars.2023.1285338 (2023).
94. Zhang, W., Yang, J., Yang, L. & Niyogi, D. Impacts of city shape on rainfall in inland and coastal environments. *Earth's Future* **10**, e2022EF002654 (2022).
95. Shin, C.-S. & Huang, B. Slow and fast annual cycles of the Asian summer monsoon in the NCEP CFSv2. *Clim. Dyn.* **47**, 529–553 (2016).
96. Salinger, M. J. et al. Coupled ocean-atmosphere summer heatwaves in the New Zealand region. *Weather Clim.* **42**, 18–41 (2023).
97. Zhang, K. et al. Increased heat risk in wet climate induced by urban humid heat. *Nature* **617**, 1–5 (2023).
98. Najibi, N. & Devineni, N. Recent trends in the frequency and duration of global floods. *Earth Syst. Dyn.* **9**, 757–783 (2018).
99. Justine, J., Monteiro, J. M., Shah, H. & Rao, N. The diurnal variation of wet bulb temperatures and exceedance of physiological thresholds relevant to human health in South Asia. *Commun. Earth Environ.* **4**, 1–11 (2023).
100. Fontaine, B., Janicot, S. & Monerie, P.-A. Recent changes in air temperature, heat waves occurrences, and atmospheric circulation in Northern Africa. *J. Geophys. Res. Atmos.* **118**, 8536–8552 (2013).
101. Russo, S., Marchese, A. F., Sillmann, J. & Immé, G. When will unusual heat waves become normal in a warming Africa? *Environ. Res. Lett.* **11**, 054016 (2016).
102. Ivanovich, C., Anderson, W., Horton, R., Raymond, C. & Sobel, A. The influence of intraseasonal oscillations on humid heat in the Persian Gulf and South Asia. *J. Clim.* **35**, 4309–4329 (2022).
103. Hunt, B. G. A climatology of heat waves from a multimillennial simulation. *J. Clim.* **20**, 3802–3821 (2007).
104. Russo, S., Sillmann, J. & Fischer, E. M. Top ten European heatwaves since 1950 and their occurrence in the coming decades. *Environ. Res. Lett.* **10**, 124003 (2015).
105. Brugge, R. Heatwaves and record temperatures in North America, June 1994. *Weather* **50**, 20–23 (1995).
106. Udy, D. G., Vance, T. R., Kiem, A. S., Holbrook, N. J. & Abram, N. Australia's 2019/20 Black Summer fire weather exceptionally rare over the last 2000 years. *Commun. Earth Environ.* **5**, 1–13 (2024).
107. Murugesan, G. P. et al. Decoding the dynamics of climate change impact: temporal patterns of surface warming and melting on the Nivlisen Ice Shelf, Dronning Maud Land, East Antarctica. *Remote Sens.* **15**, 5676 (2023).
108. Lyon, B. Southern Africa summer drought and heat waves: observations and coupled model behavior. *J. Clim.* **22**, 6033–6046 (2009).
109. Salinger, M. J. et al. The unprecedented coupled ocean-atmosphere summer heatwave in the New Zealand region 2017/18: drivers, mechanisms and impacts. *Environ. Res. Lett.* **14**, 044023 (2019).
110. Martínez, M. L. et al. The coasts of our world: ecological, economic and social importance. *Ecol. Econ.* **63**, 254–272 (2007).
111. OECD. *Urban Population by City Size* https://www.oecd.org/en/data/indicators/urban-population-by-city-size.html (2014).
112. Keellings, D. & Moradkhani, H. Spatiotemporal evolution of heat wave severity and coverage across the United States. *Geophys. Res. Lett.* **47**, e2020GL087097 (2020).
113. Gershunov, A. & Guirguis, K. California heat waves in the present and future. *Geophys. Re. Lett.* **39**, 18710 (2012).
114. Dasgupta, S. et al. Heat stress and the labour force. *Nat. Rev. Earth Environ.* https://doi.org/10.1038/s43017-024-00606-1 (2024).
115. Fan, Y. & McColl, K. A. Widespread outdoor exposure to uncompensable heat stress with warming. *Commun. Earth Environ.* **5**, 1–13 (2024).
116. Ting, M. et al. Contrasting impacts of dry versus humid heat on US corn and soybean yields. *Sci. Rep.* **13**, 710 (2023).
117. Dunn, R. J. H., Willett, K. M., Parker, D. E. & Mitchell, L. Expanding HadISD: quality-controlled, sub-daily station data from 1931. *Geosci. Instrum. Methods Data Syst.* **5**, 473–491 (2016).
118. Coffel, E. D., Horton, R. M. & Sherbinin, A.de Temperature and humidity based projections of a rapid rise in global heat stress exposure during the 21st century. *Environ. Res. Lett.* **13**, 014001 (2017).
119. NOAA. Global Surface Summary of the Day—GSOD https://www.ncei.noaa.gov/metadata/geoportal/rest/metadata/item/gov.noaa.ncdc:C00516/html (2023).
120. Menne, M. J., Durre, I., Vose, R. S., Gleason, B. E. & Houston, T. G. An overview of the global historical climatology network-daily database. *J. Atmos. Ocean. Technol.* **29**, 897–910 (2012).
121. Durre, I., Menne, M. J., Gleason, B. E., Houston, T. G. & Vose, R. S. Comprehensive automated quality assurance of daily surface observations. *J. Appl. Meteorol. Climatol.* **49**, 1615–1633 (2010).
122. Mishra, V., Ganguly, A. R., Nijssen, B. & Lettenmaier, D. P. Changes in observed climate extremes in global urban areas. *Environ. Res. Lett.* **10**, 024005 (2015).
123. Harp, R. D. & Horton, D. E. Observed changes in interannual precipitation variability in the United States. *Geophys. Res. Lett.* **50**, e2023GL104533 (2023).
124. Ganguli, P. & Ganguly, A. R. Space-time trends in U.S. meteorological droughts. *J. Hydrol. Regional Stud.* **8**, 235–259 (2016).
125. UN (United Nations). *World Urbanization Prospects 2018: Online Edition*. https://population.un.org/wup/Download/ (2018).
126. Buzan, J. R., Oleson, K. & Huber, M. Implementation and comparison of a suite of heat stress metrics within the Community Land Model version 4.5. *Geosci. Model Dev.* **8**, 151–170 (2015).

127. Dong, J., Brönnimann, S., Hu, T., Liu, Y. & Peng, J. GSDM-WBT: global station-based daily maximum wet-bulb temperature data for 1981–2020. *Earth Syst. Sci. Data* **14**, 5651–5664 (2022).
128. Kopp, R. Function to calculate wetbulb temperature Available at: https://github.com/bobkopp/WetBulb.m/blob/main/WetBulb.m (2016). (Accessed November 2023).
129. Rogers, C. & Warren, R. Fast and accurate calculation of wet-bulb temperature for humid-heat extremes, EGU General Assembly 2024, Vienna, Austria, 14–19 April 2024, https://doi.org/10.5194/egusphere-egu24-14205 (2024).
130. Russo, S. et al. Magnitude of extreme heat waves in present climate and their projection in a warming world. *JGR Atmos.* **119**, 500–512 (2014).
131. Lo, S.-H., Chen, C.-T., Russo, S., Huang, W.-R. & Shih, M.-F. Tracking heatwave extremes from an event perspective. *Weather Clim. Extremes* **34**, 100371 (2021).
132. Domeisen, D. I. et al. Prediction and projection of heatwaves. *Nat. Rev. Earth Environ.* **4**, 1–15 (2022).
133. Xu, L., Wang, A., Yu, W. & Yang, S. Hot spots of extreme precipitation change under 1.5 and 2° C global warming scenarios. *Weather Clim. Extremes* **33**, 100357 (2021).
134. Czajkowski, J., Villarini, G., Montgomery, M., Michel-Kerjan, E. & Goska, R. Assessing current and future freshwater flood risk from North Atlantic tropical cyclones via insurance claims. *Sci. Rep.* **7**, 41609 (2017).
135. Rowe, S. T. & Villarini, G. Flooding associated with predecessor rain events over the Midwest United States. *Environ. Res. Lett.* **8**, 024007 (2013).
136. Wang, P. et al. Increasing compound hazards of tropical cyclones and heatwaves over Southeastern Coast of China under climate warming. *J. Clim.* **36**, 2243–2257 (2023).
137. Navale, A. & Karthikeyan, L. Soil moisture-precipitation feedbacks in pre- and post-monsoon landfalling tropical cyclones in Bay of Bengal. *Q. J. R. Meteorol. Soc.* **149**, 2433–2453 (2023).
138. Yang, L. et al. Extreme events and probability analysis along the United States east coast based on high spatial-coverage reconstructed storm surges. *Geophys. Res. Lett.* **50**, e2023GL103492 (2023).
139. Nogaj, M., Yiou, P., Parey, S., Malek, F. & Naveau, P. Amplitude and frequency of temperature extremes over the North Atlantic region. *Geophys. Res. Lett.* **33**, 2005GL024251 (2006).
140. Frahm, G., Junker, M. & Schmidt, R. Estimating the tail-dependence coefficient: properties and pitfalls. *Insurance Math. Econ.* **37**, 80–100 (2005).
141. Mardia, K. V. Statistics of directional data. *J. R. Stat. Soc. Ser. B Stat. Methodol.* **37**, 349–371 (1975).
142. Demirel, M. C., Booij, M. J. & Hoekstra, A. Y. Impacts of climate change on the seasonality of low flows in 134 catchments in the river Rhine basin using an ensemble of bias-corrected regional climate simulations. *Hydrol. Earth Syst. Sci.* **17**, 4241–4257 (2013).
143. Burn, D. H. & Whitfield, P. H. Changes in flood events inferred from centennial length streamflow data records. *Adv. Water Resour.* **121**, 333–349 (2018).
144. Gudmundsson, L., Leonard, M., Do, H. X., Westra, S. & Seneviratne, S. I. Observed trends in global indicators of mean and extreme streamflow. *Geophys. Res. Lett.* **46**, 756–766 (2019).
145. Schleussner, C.-F., Donges, J. F., Donner, R. V. & Schellnhuber, H. J. Armed-conflict risks enhanced by climate-related disasters in ethnically fractionalized countries. *Proc. Natl. Acad. Sci. USA* **113**, 9216–9221 (2016).
146. Zhang, L. & Singh, V. P. *Copulas and Their Applications in Water Resources Engineering* (Cambridge University Press, 2019).
147. Genest, C., Ghoudi, K. & Rivest, L.-P. A semiparametric estimation procedure of dependence parameters in multivariate families of distributions. *Biometrika* **82**, 543–552 (1995).
148. Chowdhary, H. & Singh, V. P. Reducing uncertainty in estimates of frequency distribution parameters using composite likelihood approach and copula-based bivariate distributions. *Water Resour. Res.* **46**, 2009WR008490 (2010).
149. Genest, C., Rémillard, B. & Beaudoin, D. Goodness-of-fit tests for copulas: a review and a power study. *Insurance: Math. Econ.* **44**, 199–213 (2009).
150. Hurvich, C. M. & Tsai, C.-L. Regression and time series model selection in small samples. *Biometrika* **76**, 297–307 (1989).

Acknowledgements

The work received funding from the first author's Women Involvement in Science and Engineering Research (WISER) fellowship from Indo-German Science and Technology Centre (IGSTC), with funding ID: IGSTC/WISER 2022/PG/47/2022-23/514. Dr. Ganguli is in a visiting professorship position (from August 2024 to February 2025) funded by USIEF's Fulbright-Kalam research fellowship at Civil and Environmental Engineering at Princeton University, NJ, USA. The generous support from the foundation is deeply acknowledged.

Author contributions

P.G. collected the data, performed the analysis, and prepared the first draft of the manuscript. Both P.G. and B.M. defined the problem and designed the experiments. All authors reviewed and wrote the manuscript.

Competing interests

The authors declare no competing interests.

Additional information

Supplementary information The online version contains supplementary material available at https://doi.org/10.1038/s41612-025-01023-x.

Correspondence and requests for materials should be addressed to Poulomi Ganguli.

Reprints and permissions information is available at http://www.nature.com/reprints